Deanship of Graduate Studies
Al – Quds University

Optically Induced Magnetization Dynamics in Magnetic Films and Microstructures

Baha'alddin Mahmoud Abureesh

M.Sc. Thesis

Jerusalem – Palestine

December 2014

Deanship of Graduate Studies
Al – Quds University

Optically Induced Magnetization Dynamics in Magnetic Films and Microstructures

Baha'alddin M. Abureesh

A thesis submitted in partial fulfillment of requirement
for the degree of Master of Science in Physics

Supervisors

Prof. Salman M. Salman
Physics Department, Al-Quds University, Palestine

Prof. Claus M. Schneider
Peter Grünberg Institute, Electronic Properties (PGI-6)
Jülich Research Center, Germany

Jerusalem – Palestine

December 2014

Deanship of Graduate Studies
Al – Quds University

Thesis Approval

Optically Induced Magnetization Dynamics in Magnetic Films and Microstructures.

Baha'alddin M. Abureesh.
Registration No: 21110561.

Supervisors
Prof. Salman M Salman, Physics Al-Quds University, Palestine.
Prof Claus M. Schneider, Peter Güunberg Institute-PGI-6, FZ Jülich, Germany.

Master thesis submitted and accepted, / / 2014.

The name and signature of examining committee member are as follows:
1- Head of the committee: Prof. Salman M Salman Signature: ..……..…

2.Internal Examiner: Dr.Musa AbuTai Signature: .....

3.External Examiner: Dr.Jamal Ghaboun Signature: .....

Jerusalem- Palestine
December 2014

Dedication

I lovingly dedicate this thesis to my family for their endless love, support and encouragement.

Declaration

I, Baha'alddin M. Abureesh, declare that this thesis "**Optically Induced Magnetization Dynamics in Magnetic Films and Microstructures**" and the work presented in it are my own and has been generated by me as the result of my own original research and that it has not been submitted earlier elsewhere.

I confirm that this work was done under the supervision of Professor Salman M. Salman from the Physics Department, Alquds University, Palestine, and Prof Claus M. Schneider the head of Peter Grünberg Institute, Electronic Properties (PGI-6), Jülich Research Center, Germany.

Baha'alddin M. Abureesh
Jerusalem - Palestine
December 2014

Acknowledgements

First and foremost, I would like to thank **Allah**, due to his blessings I could finish my thesis.

I would like to thank my beloved **parents and family** for their encouragement who are so supportive to me throughout my life.

It is important to thank those people who have contributed to the development of this thesis. Thanks, first of all, to **Prof. Salman M. Salman** for giving me a chance to conduct the practical part of this thesis within the framework collaboration between Al-Quds University and Research Center Jülich*. Thanks and appreciation to **Prof. Claus M. Schneider** for supporting my work in every sense and providing excellent working conditions in his institute.

Last but not least, I also thank **my friends** and **my teachers** (too many to list here, but you know who you are!) for providing support. I would like to especially thank **Sadam Hazaimeh** for being supportive throughout my time in Germany.

Bahaʼalddin M. Abureesh

*****This project is the part of a collaborative effort under the SCP-1 of the framework collaboration between Jülich research Center, Germany, and Alquds University, Palestine, and coordinated by Professors Claus Schneider the head of Peter Grünberg Institute, Electronic Properties (PGI-6) and Salman M Salman from Physics and Director of Alquds Jülich Cooperation Program at Alquds University.

Abstract

In the present work the magnetic dynamics of various magnetic films were examined using the magneto-optic Kerr effect (MOKE). At first, the magneto-optic Kerr-effect was employed to study the effect of *thickness*, *size* and *ratio* of Ni on the magnetic behavior of Ni.

The magnetic dynamics of $\mathbf{Co_{65}Pd_{35}}$ films we studied using Magnetic Force Microscopy (MFM), the Superconducting Quantum Interference Device (SQUID), and MOKE magnetometer.

The coercivity of lithography $\mathbf{Co_{65}Pd_{35}}$ circular dot arrays of different separations between dots were studied using focused MOKE. The coercivity of the dots was found to depend on the separation, indicating the effect of the interdot dipole coupling on the magnetization reversal process.

Understanding the loss of magnetic order and the microscopic mechanisms involved in laser induced magnetization dynamics is one of the most challenging topics in today's magnetism research. We used the time resolved magneto-optical Kerr effect (pump- probe technique) in polar Kerr geometry to study the ultrafast demagnetization dynamics of $Co_{65}Pd_{35}$ and $\mathbf{Ni_xPd_{100-x}}$ films. The effect of the geometry was evident and results were compared with **the Koopmans et al model [Koopmans et al, 2010]** yielding agreements and indications of dependence on the Pd component.

Contents **page**

List of Tables

List of Figures

List of Abbreviations

AOM	Acousto-optic modulators
BBO	Beta-barium borate crystal
BPMR	Bit patterned magnetic recording
CoPd	Cobalt Palladium
H_c	Coercivity field
ϕ_K	Complex Kerr-angle
G_{es}, G_{ls}, G_{el}	Coupling constants between electron-lattice-spin
$\theta_{W\,eiss}$	Curie-Weiss constant
Δt	Delay time between the pump and peob-beam
N_a	Demagnetization factor parallel to the easy-axis
τ_M	Demagnetization time
$\varepsilon(\omega)$	Dielectric tensor
DPSS	Diode pumped solid state
ε_{ex}	Exchange energy
FM	Ferromagnetic layers
FWHM	Full-width at half-maximum
GMR	Giant magneto resistance
C_e	Heat capacity of lattice system
C_l	Heat capacity of lattice system
C_s	Heat capacity of spin system
HAMR	Heat-assisted magnetic recording
ε_K	Kerr ellipticity
Θ_k	Kerr rotation
LBO	Lithium triborate
F	Magnetic force
MFM	Magnetic force microscopy
MRAM	Magnetic random access memory
χ	Magnetic susceptibility

MOKE	Magneto-optical Kerr effect
E_m	Magneto static energy
MBE	Molecular Beam Epitaxy
$NdYVO_4$	Neodymium yttrium vanadate
NiPd	Nickel Palladium
NM	Nonmagnetic layer
μ_0	Permeability of free space
PGI	Peter Grünberg Institute
PMMA	Polymethyl methacrylate
τ_E	Recovery time
r_{pp}	Reflection coefficient for p-polarized light
M_R	Remanent magnetization
Δz	Rising displacement
M_s	Saturation magnetization
ε_d	Stray field energy
SQIUD	Superconducting quantum interference device
3TM	Three temperature model
TBP	Time-bandwidth product
Ti:Sa	Titanium-sapphire
TMR	Tunneling magneto resistance
X-PEEM	X-ray photoemission electron microscopy
x_0	Zero-delay

Chapter 1 Introduction

Scientific understanding of magnetism started with the development of modern industrialization. The most critical development to magnetism, or electromagnetism in general, was made by the experimentalist Michel Faraday together with the theoretician James Clerk Maxwell. Faraday observed that light changes polarization when it propagates through magnetized material **[Stöhr, Siegmann, 2006]**. The same magneto-optical effect in reflection also exists and was discovered later by John Kerr **[Hubert, Schäfer, 2000]**, which is an important basis for studying magnetism using optical methods.

1.1 Technological Motivations

The study of magnetization processes in magnetic materials has seen significant progress in the last sixty years. The focus was on applications in magnetic recording technology. Currently, magnetic storage devices, such as hard-disks, require the knowledge of the "microscopic" phenomena occurring within magnetic recording medium. The magnetic medium is made of ferromagnetic materials with preferred magnetization direction. This means the magnetization direction tends to spontaneously align. The magnetic recording technology exploits the magnetization of ferromagnetic media to store information.

1.1.1 Magnetic Core Memory (MCM)

The first example of modern magnetic storage devices was the MCM realized by An Wang, a Harvard physicist and the co-founder of the computer company Wang Laboratories in 1950. This technique became predominant in the computer memories industry in the early 1960s. It was replaced by the integrated silicon RAM chips in 1970s, because the lifetime of the MCM was relatively short.

MCM consists of a matrix of small cores, as shown in figure 1.1. These are made of ferrite ceramic material with a high degree of magnetic remanence. The working principle of MCM is very simple. Each core is basically a bistable unit, capable of storing one binary bit (0 or 1). Figure 1.1a illustrates the writing mechanism of the IBM Core Storage Module. The writing process is realized by applying currents in two wires. Figure 1.1b shows opposite magnetization states as white and black arrows. The binary information can be

stored by passing the current in one direction or another. The third wire is used to read out of the bits. **[Stöhr, Siegmann, 2006]**.

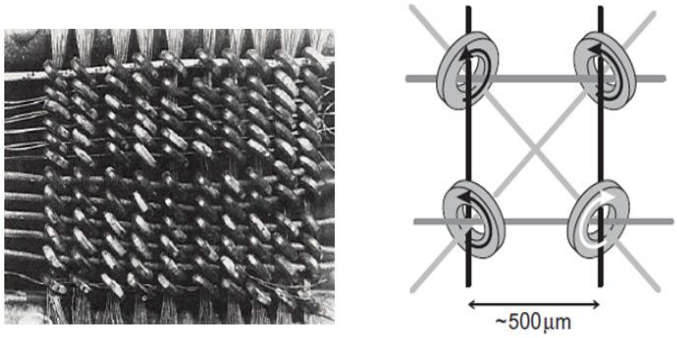

(a) **(b)**

Figure 1.1: (a) The first magnetic core memory used in the IBM 405 Alphabetical Accounting Machine. (b) Writing mechanism of magnetic cores memory(taken from [Stöhr, Siegmann, 2006]).

After MCM, magnetic tapes and floppy disks were used, but the most widespread magnetic storage device is certainly the hard-disk.

1.1.2 The modern recording process: hard disks and MRAMs

The applications of magnetism are present in different devices like hard disks read and write heads. These devices are the key technology for non-volatile massive data storage in computer systems.

To keep pace with the increasing demands for higher data storage capacities and data transfer rates, the recording industry faces the challenge of growth in the magnetic functional materials research. A convincing example is the discovery of the giant magneto resistance (GMR) by prof. Albert Fert and prof.Peter Grünberg. GMR refers to the large changes in the electrical resistance observed in thin magnetic films, like multilayers and trilayers depending on their magnetic properties. Basic GMR structure is composed of two Ferromagnetic Layers (FM) separated by a None-Magnetic layer (NM), are shown in figure 1.2. The electrical resistance (R) changes dramatically when the magnetization orientation of one magnetic layer is reversed. The magnetization direction can be controlled, by applying an external magnetic field. The effect is based on the dependence of electron scattering on the spin orientation. When the middle layer in figure 1.2 is an ultra thin layer

of insulator the effect relies on the possibility for electrons to tunnel between the two magnetic layers, hence it is called tunneling magneto resistance (TMR) **[Longa, 2008] [Shinjo, 2009]**.

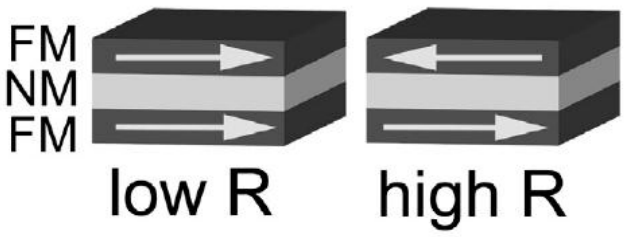

Figure 1.2: Basic GMR structure composed of a none-magnetic layer (NM) sandwiched between two ferromagnetic layers (FM): the electrical resistance experienced by an electron traveling through the stack depends on the relative orientation of the magnetization of the two ferromagnets [Kampen, 2003]).

GMR can be (and is) used to build sensitive devices for many applications in magnetic recordings. Ten years after its discovery, GMR-based read heads for computer hard disks were already commercially available **[Longa, 2008]**. The principle of the modern hard disk is depicted in Figure 1.3. The recording medium is a flat thin-film magnetic material. The read and write heads are separate in modern devices. In order to write a bit, a current pulse is applied to the write head, generating a magnetic field to change the magnetization state of the recording medium. The recording medium is made of elements that have discrete preferred magnetization directions. This means the magnetization direction tends to flip in one direction (‘1’ direction) or the opposite (‘0’ direction). The GMR and TMR sensors are used in the read head to detect the direction of the field from magnetic medium. This field is large enough to reverse the magnetization direction of the free layer (can change easily) and thus increase the resistance of the head. More precisely, when the magnetizations of the free and pinned layers are parallel, the electrical resistance is minimum. Conversely, the antiparallel magnetization of the two layers yields maximum resistance. The change between the two states is transferred to an analog voltage output signal representing the information recorded **[Fratta, 2012].**

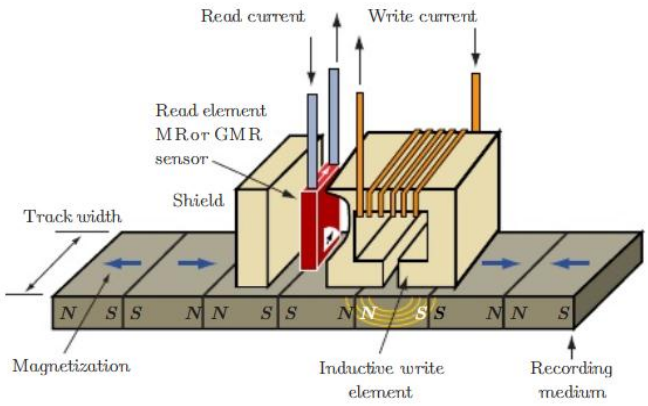

Figure 1.3: Schematic representation of the read and write processes of modern longitudinal recording hard disk (taken from [Fratta, 2012]).

Another emerging application is the so-called magnetic random access memory (MRAM composed of an array of TMR elements as shown in Figure 1.4. In a typical MRAM device, the binary information is recorded as two opposite orientations of the magnetization of the top layer of TMR element connected to the crossing points of two perpendicular arrays of parallel conducting lines (bit lines and word lines in Figure1.4).

For writing, current pulses are sent through lines, and only at the crossing point of these lines the resulting magnetic field is high enough to orient the magnetization of the free layer. For reading, the resistance between the two lines connecting the addressed cell is measured **[Chappert et al, 2007]**.

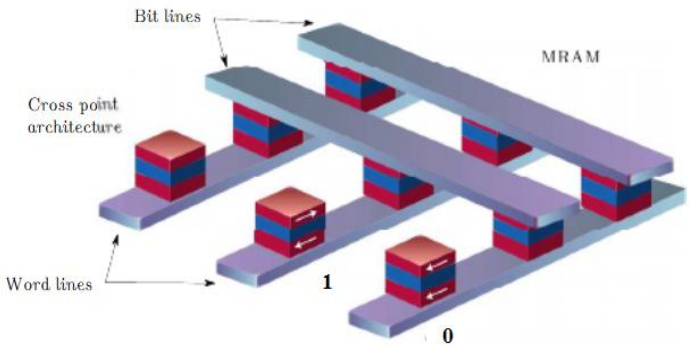

Figure 1.4: Typical array structure for magnetic random access memories (MRAMs) [Chappert et al, 2007].

1.1.3 The quest for smaller and faster

Magnetic properties of patterned elements are of increasing interest. Understanding the magnetic material size and shape reduced and placed in a regular array is of great importance fundamentally and for eventual applications in recording media and nonvolatile memories.

Some of the major challenges facing modern recording technology, currently include higher areal density; improved thermal stability of magnetized bits; and increasing read/write speed.

In 1956, the first commercial hard disk drive was introduced by IBM with only 4.4 MB/in^2 of storage density. Recently, the density of hard disks reached over 250GB/in^2, and densities as high as 520 GB/in^2 have been demonstrated in the laboratory. **[Malaika, Nicola, 2011]**. The evolution of the magnetic storage areal density is given in figure 1.5.

Since 1997, when the GMR heads appeared, recording density improved by 100% annually until dropping to 30% in 2001 due to a slowing in the pace of advancement.

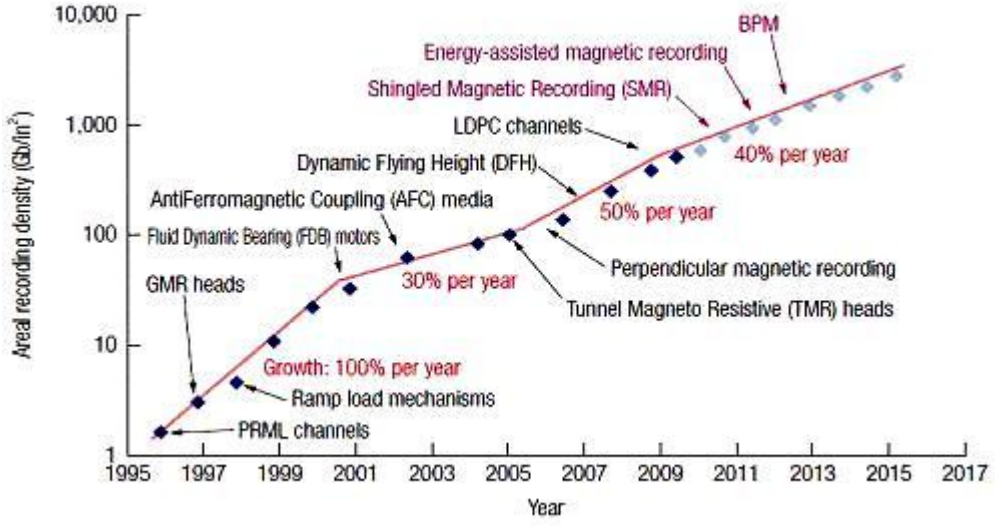

Figure 1.5: Exponential growth of the hard disks areal density. Since 1997 when GMR heads appeared, the rate doubled annually until 2001 when the increase dropped to only 30% due to lake of fundamental advancement. The practical application of the perpendicular magnetic recording method restored the rate of improvement to 50% in 2005[Masakatsu et al, 2013].

The introduction of perpendicular recording in 2005 has largely increased the areal density. With the size of the "bit" becomes smaller and smaller, hard disk drives are now approaching the fundamental physics limit of superparamagnetism, in which random reversal of the magnetization occurs due to thermal fluctuations. Perpendicular recording and other techniques, such as heat-assisted magnetic recording (HAMR), bit patterned magnetic recording (BPMR) and microwave assisted magnetic recording, are employed to push storage density to about 1 Tb/in^2. **[Masakatsu et al, 2013]**.

Over the last decade, data storage devices and sensors are getting smaller and access to information faster. For example, as the size of digital universe increases from 300 Exabyte's in 2005 to about 40,000 Exabyte's **[Gantz, Reinsel, 2012]**, it is important to maintain a fast development of the capacity of the magnetic elements. A larger capacity with the same physical dimension means smaller magnetic elements, and this needs knowledge about their magnetic properties. Experimental techniques that proved useful for understanding magnetic properties, include magnetic force microscopy (MFM), magneto-optical Kerr effect (MOKE), superconducting quantum interference device (SQIUD), magnetic transmutation x-ray microscopy, and x-ray photoemission electron microscopy(X-PEEM).

Increasing the read and write speed of recording devices into the GHz regime requires a detailed study of the magnetization dynamic on the picosecond time scale. To achieve this objective experiments using the pump-probe technique have been introduced. The basic principle is to excite the magnetic system and detect the response after a time delay. There three ways to excite the magnetic system, as shown in figure 1.6: magnetic-field induced perturbation H(t), laser heating (thermal excitation focuses a laser pulse directly to magnetic sample T(t) and spin-selective excitation by polarized light S(t). Similarly, the detection of the induced magnetic dynamic can be realized by magneto-optical Kerr effect (MOKE) **[Koopmans, 2003]**.

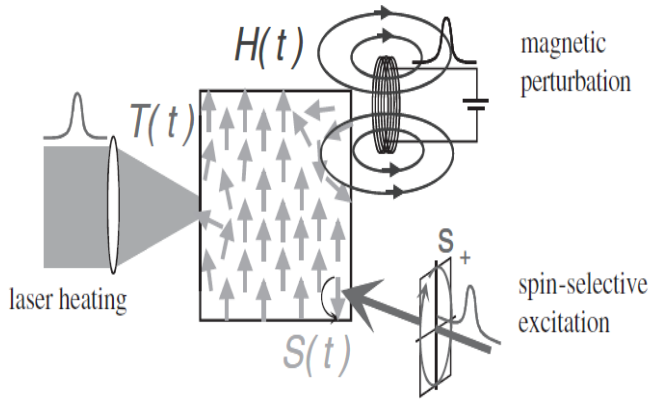

Figure 1.6: Schematic illustration of three excitation methods.

In 1996, the group of Beaurepaire found that excitation by an intense femtosecond laser pulse can induce demagnetization in Nickel thin films on a sub picosecond timescale **[Beaurepaire et al, 1996].** This discovery lead to a growing interest in the field of laser induced magnetization dynamics, as a possibility to manipulate spins on the femtosecond timescale with many potential applications. Many experimental efforts were made to confirm this finding in Nickel and a wide range of magnetic materials. For example Fe**[Carpene et al, 2008] [Kampfrath et al, 2002]** or Co **[Koopmans et al, 2010] [Carva et al, 2011]**, magnetic semiconductors **[Wang et al, 2008]**, and dielectrics **[Kimel et al, 2002]**.

1.2 About This Work

1.2.1 Place of research (Jülich Research Center, Peter Grünberg Institute)

The experimental work presented in this thesis was performed at the Research Center Jülich in Germany, specifically in Peter Grünberg Institute (PGI) (see figure 1.7).

The Peter Grünberg Institute (PGI) was established in 2011 as a merger of the Institute of Solid State Research (IFF) and the Institute for Bio- and Nano systems (IBN) which have been dealing with electronic phenomena, materials, and devices. Named after Peter Grünberg, the first Nobel laureate in the Jülich research center, the institute dedicates itself

to fundamental research in the field of information technology and related areas. Major topics of the PGI research are the electronic properties of solid state structures ranging.

Figure 1.7: The Peter Grünberg Institute.

The Peter Grünberg Institute comprises the divisions: Quantum theory of materials, theoretical nano-electronics, and functional nanostructures at surfaces, scattering methods, electronic properties, electronic materials, and bioelectronics and semiconductor nano - electronics. The work was performed at the electronic properties institute PGI-6. The interrelations between electronic structure and physical properties such as magnetism and magnetic phenomena are explored by applying, for example, synchrotron radiation techniques. Systems of interest range from thin film systems, quantum wires and dots to molecules. Keywords here are nanosciences, spintronics, quantum computing, and giant magneto resistance.

The PGI is a valuable collaboration partner for more than 100 universities and research institutes worldwide. Within Germany the PGI has established close relations to scientists and research groups throughout the country, and takes a leading position as scientific partner in cooperation with industry and companies such as Agilent, Bosch, Daimler-Chrysler, Exxon Mobil, Infineon, Intel, Micron, Philips, Samsung and Thomson.

1.2.2 Overview of this research

The aim of the work presented in this thesis is to study magnetization dynamic in ferromagnetic materials. Additionally, study of ultrafast demagnetization dynamics in $Co_{65}Pd_{35}$ alloy and Ni_xPd_{100-x} alloys with different mixing ratios using time-resolved MOKE techniques.

In chapter two focus on the theoretical background, followed by a detailed discussion of the magnetization dynamics induced by optical excitations with ultra short laser pulses.

Chapter three reviews the experimental setup used. A preliminary characterization employing the magneto optic Kerr-effect was employed to get first hand information about the samples. Then a time-resolved MOKE setup in pump-probe arrangement with a temporal resolution of less than 100 fs is employed to measure demagnetization time (τ_M) in a ferromagnetic alloy and patterned element.

Chapter four summarizes the results of the work. Data from different magnetic samples will be presented.

Finally in **Chapter five** presents a summary of conclusions and recommendations for future work.

Chapter 2 Theoretical Concepts

2.1 Magnetism of Ferromagnetic Film

Even though magnetism has been known for at least 2000 years, it took until the thirties of the last century to develop a first understanding of the involved fundamental processes. Even today no complete satisfying theory exists to explain or unify the magnetic behavior of different material classes.

2.1.1 Ferromagnetism and Weiss theory

Cobalt and nickel are examples of ferromagnetic materials. In 1907, Pierre Weiss published his hypothesis **[Weiss, 1906]** that magnetic moments in ferromagnetic materials interact in a way such that each moment tries to align the others in its own direction. This hypothesis lead to the Curie Weiss law

$$\chi = \frac{C}{T\text{-}\theta_{W\,eiss}} \qquad 2.1$$

Where χ the magnetic susceptibility of the material, C is the curie constant, T is the absolute temperature and $\theta_{W\,eiss}$ is the Curie-Weiss constant, Ferromagnetic materials magnetization remains after removing the applied magnetic field. Weiss theory deduced that the existence of magnetic domains in ferromagnetic materials defines their magnetization state but it did not explain the origin of magnetic domains.

Heisenberg used quantum mechanics to describe these domains. He explained that their origins in ferromagnetic materials are the result of exchange interactions between magnetic moments. Heisenberg also showed that magnetic moments are ordered even in a demagnetized state and the domains keep consistently re-orienting during magnetization by an external magnetic field. These ordered magnetic domains stay aligned until reaching the Curie temperature when ferromagnetic properties change to paramagnetic.

The Curie-Weis law describes fairly well the observed susceptibility variation in the paramagnetic region above the Curie point, as shown in figure 2.1. Only in the vicinity of the Curie temperature a notable deviations are observed. This due to the fact that strong fluctuations of the magnetic moments close to the phase transition temperature cannot be

described by the mean field theory which was used for deriving the Curie-Weiss law. Accurate calculations predict that

$$\chi \propto \frac{C}{(T-T_C)^{1.33}} \qquad 2.2$$

at temperatures very close to T_C.**[Tsymbal, 2014]**

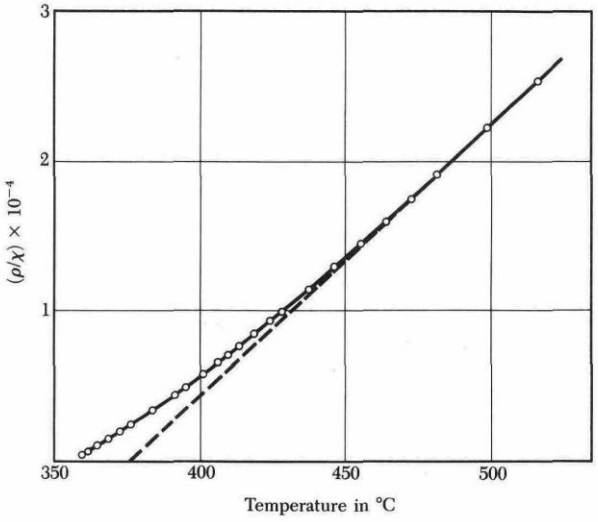

Figure 2.1: Reciprocal of the susceptibility per gram of nickel in the neighborhood of the Curie temperature (358°C). The dashed line is a linear extrapolation from high temperatures.

2.1.2 Magnetization curve (hysteresis loop)

The hysteresis loop in ferromagnetic material is caused by the magnetization reversal of the magnetic domains when an external magnetic is applied. Therefore, one can relate the magnetic characteristic of the material to its hysteresis loop properties. The following parameters can be extracted:

- Magnetization Saturation (M_s): is the value of magnetization when all the magnetic moments are aligned with the applied magnetic field.
- Magnetization Remanence (M_R): the value of the magnetization after removing the applied magnetic field.
- The coercivity (H_c): the reverse magnetic field value needed to reduce magnetization to zero. It defines the width of the hysteresis loop accordingly to the degree of the material magnetic strength. Large H_c means magnetically hard and vice versa.

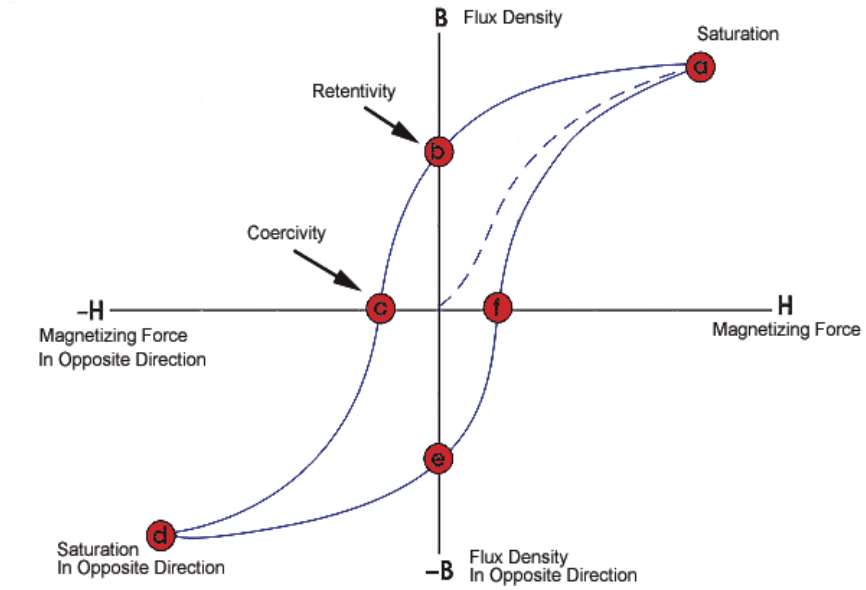

Figure 2.2: A hysteresis loop to study the magnetic characteristic of the magnetic sample. [NDT, 2013].

2.1.3 Magnetic domains

The magnetic domain of a material is a region in which all atomic magnetic moments are aligned and point in one direction. They explain the hysteresis curves behavior and why magnetization goes from the saturation value to zero. Within each domain the magnetization is uniform and equals to the spontaneous magnetization (is the appearance of an ordered magnetization at zero applied magnetic field in ferromagnetic material below T_C) but the distribution of all domains tends to be random for para magnetism and for ferromagnetism with some residue below the Curry temperature that needs a reverse magnetic field to remove it.

The average magnetization of a specimen is not equal to the spontaneous magnetization but will be within the range from zero to Ms. The first experimental evidence for magnetic domains was the Sixtus and Tonks experiments when Barkhausen observed the magnetization reversal in nickel wires in a single large jump between two opposite saturated states **[Sixtus and Tonks, 1931]**. In 1932, Bitter obtained the first images of the magnetic domains using a powder technique **[Bitter, 1932]**. The occurrence and the shape of domains depend on the relative strengths of the exchange and stray field energies **[Kobs, 2013]**.

Exchange Energy

The fundamental explanation of exchange energy lies in the Coulomb interaction and the Pauli Exclusion Principle. The exchange interaction aligns or anti-aligns the spins in a magnetic material. Orbital moments are neglected, as they are assumed to be quenched by averaging the angular momentum to zero. Using the Heisenberg-Dirac approximation the exchange energy has a form.

$$H_{exch} = -2\Sigma_{ij} J_{ij} S_i S_j \qquad 2.3$$

Where J_{ij} is positive for ferromagnets and the spins are completely localized. When the spin magnetic moments of the adjacent atoms i and j are oriented at relative angle φ_{ij}, the exchange energy between the two moments is

$$\Sigma_{ij} E_{ij} = -2\Sigma_{ij} J S^2 Cos\varphi_{ij} \approx J S^2 \Sigma_{ij} \varphi_{ij}^2 \qquad 2.4$$

Where $\varphi_{ij} << 1$, J is the exchange integral and S is the total spin quantum number of each atom **[Belov, 2004]**.

The **demagnetizing field H_d**, also called the **stray field**, is the magnetic field (H-field) generated by the magnetization in a magnet. It reflects the tendency to act on the magnetization so as to reduce the total magnetic moment. It gives rise to *shape anisotropy* in ferromagnets with a single magnetic domain and to magnetic domains in larger ferromagnets. **The Stray field energy** is given by:

$$\varepsilon_d = -\frac{\mu_0}{2} \int_{Sample} \vec{H}_d * \vec{m}\, dV \qquad 2.5$$

The stray field depends on the shape of the specimen. A good approximation for many situations is to assume a general ellipsoidal shape for the sample. Magnetic domains exist in order to reduce the magneto-static energy of the system **[Landau and Lifshitz, 1935]**. The magneto static energy can be evaluated as

$$E_m = \frac{\mu_0}{2} \int H_{str}^2 \, dV \qquad 2.6$$

Where μ_0 is the permeability of free space. The interaction of dipoles is much weaker than the exchange interaction that occurs in the short range distance, but for the long range the dipoles interaction is dominant. The uniformly magnetized specimen shown in Fig. 2.3a has

a large magneto-static energy associated with it **[Kittel, 1949]**. This is due to the presence of magnetic poles at the surface of the specimen generating a demagnetizing field H_d.

The magnitude of H_d depends on the geometry and in general, it points opposite to the direction of magnetization of the specimen. For samples with large length /diameter ratio and magnetized along the long axis, the demagnetizing field H_d and the magneto-static energy will be low. The magnetic domain is divided into two parts as shown on Figure 2.3 (b) and that reduces the magneto-static energy by half. Figures 2.3d and 2.3e show a closure domain structure where the magneto-static energy is close to zero **[Belov, 2004]**.

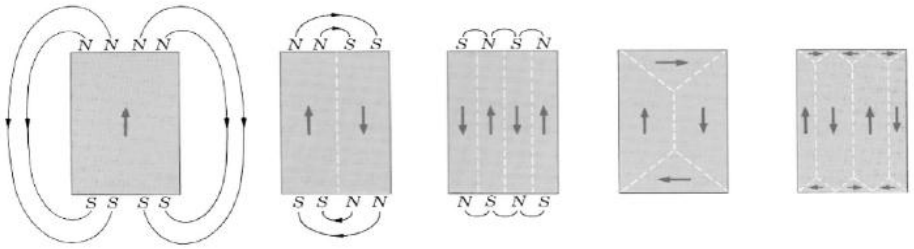

(a) (b) (c) (d) (e)

Figure 2.3: Schematic description of the reduction of magneto static energy by formations of domains, (a) 1 domain, (b) 2 domains, (c) 4 domains (d) and (e) closure domains [Bader, 2006].

2.1.4 Shape anisotropy

For a small patterned magnetic structure, the sample can be saturated along the direction of the applied magnetic field to give a single magnetic domain. The sample can retain its single domain magnetization or form sub-domains without the applied magnetic field, given that the size and shape is less than the critical value of the material. Likewise, formed domain patterns are more favorable due to the shape and size effect on the sample magneto-static energy. The shape anisotropy energy density can be derived from the stray field magneto-static energy produced by the magnetic dipoles on the sample surface:

$$\varepsilon_s = \frac{1}{2}\mu_0 M_S^2 (N_a \cos^2\theta + N_b \sin^2\theta) \qquad 2.7$$

Where N_a is the demagnetization parallel to the easy-axis, θ is the angle between the easy axis and the magnetization and N_b is the demagnetization perpendicular to the easy-axis of the sample **[Hujan, 2013]**. Figure 2.4 shows circular dot shape sample, where the more favorable magnetization direction is along the long axis of the sample. In addition, the

saturation magnetic field along the short axis is higher than the filed along the easy axis due to the higher magneto-static energy for the short axis.

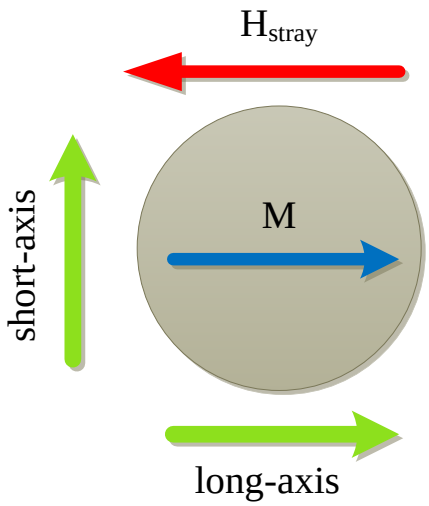

Figure 2.4: Schematic of a circular dot shaped sample showing its long and short axes.

2.1.5 The dipole-dipole (dipolar) interaction in the magnetic array

The principal coupling inside the magnetic dot array is the dipolar interaction, usually defined as a long-range force. There are other types of coupling, at shorter range, such as the interaction across the interface between a ferromagnetic and an antiferromagnetic spin system (exchange coupling); or between two ferromagnetic materials through the magnetic interlayer (interlayer exchange coupling).

The dipolar interaction depends on a term $1/r^3$ with r the distance between the centers of the magnetic elements. For a direction along which the spacing between the magnets is sufficiently reduced, the magneto static coupling becomes an anisotropic, having minimum energy when the dipoles are aligned with it (easy axis) and maximum energy when aligned perpendicular to it (hard axis). The effects of the interaction are many: e.g., change of the saturation and coercivity field. Several experiments **[Xu et al, 2001], [Sun et al, 2011]** and theoretical models **[Zhang et al, 2005]** were made to understand the dots dipolar interaction.

2.2 Magneto-Optical Kerr-Effect (MOKE)

2.2.1 Phenomenological review

The first very useful technique to measure the magnetic state of a sample is the magneto-optical Kerr effect (MOKE). It provides a fast and easy way by reasonably simple setup. It is composed of a polarized light source and an analyzer sensitive to the polarization of light variations. In addition, the MOKE technique is well suited for time-resolved measurements, using state-of-the-art ultra fast lasers.

The magneto-optical Kerr effect was discovered by John Kerr in 1877. He observed that the polarization vector of linearly polarized light rotates by a small angle Θ_k when reflected from a magnetized sample (a polished electromagnet pole) **[Weinberger, 2008]**. Augusto Righi discovered in 1886, that the reflected light is generally elliptically polarized. The Kerr-effect is described by the complex Kerr-angle ϕ_K given by

$$\phi_K = \Theta_k + i\varepsilon_K \qquad 2.8$$

With Θ_k the rotation angle, and $\varepsilon_k = b/a$ the ellipticity; a and b the long and short ellipse axes (see figure 2.5).

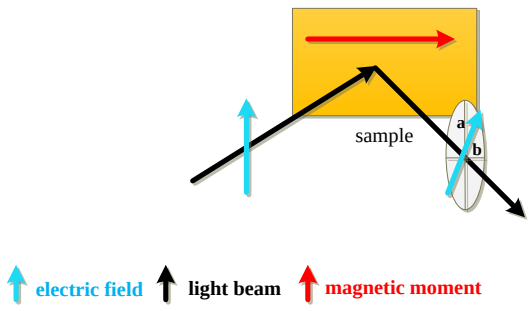

Figure 2.5: Schematic of the polarization change of a linearly polarized beam in MOKE.

The rotation of the axis of polarization is due to unequal coefficients of reflection for left- and right-circularly polarized light, and the ellipticity is due to the unequal absorption coefficient of the reflecting material **[Oppeneer, 2000]**. The value of the rotation angle depends on the projection of the magnetization vector M onto the propagation vector of the incoming light.

2.2.2 Calculation of the complex Kerr angle in MOKE geometries

The dielectric tensor of the optically isotropic material can be given by:

$$\varepsilon(\omega) = \begin{pmatrix} \varepsilon_{xx} & 0 & -\varepsilon_{xz} \\ 0 & \varepsilon_{yy} & 0 \\ 0 & 0 & \varepsilon_{zz} \end{pmatrix} \qquad 2.9$$

With magnetization M, the sample becomes optically anisotropic. The off-diagonal elements reflect the effect of the magnetization:

$$\varepsilon(\omega) = \begin{pmatrix} \varepsilon_{xx} & \varepsilon_{xy} & -\varepsilon_{xz} \\ -\varepsilon_{xy} & \varepsilon_{yy} & \varepsilon_{yz} \\ \varepsilon_{xz} & -\varepsilon_{yz} & \varepsilon_{zz} \end{pmatrix} \qquad 2.10$$

Note that the time-reversal symmetry is broken with magnetization:

$$\varepsilon_{ij}(M) = -\varepsilon_{ij}(M) \qquad 2.11$$

The propagation of the light wave can be described by Fresnel's equation

$$(n^2 \underline{\underline{1}} - \underline{\underline{\epsilon}} - \underline{n} \cdot \underline{n}^T) \cdot \underline{E} = 0. \qquad 2.12$$

$\underline{n}$ denotes the complex refractive index

$$\underline{n} = \tilde{n} + i\tilde{k} \qquad 2.13$$

This is a frequency-dependent material property. It combines the refractive index $\tilde{n}$ (proportional to the phase velocity) with the extinction coefficient $\tilde{k}$.

In the following, three Kerr-geometries will be presented, and the complex Kerr-angle will be derived for the polar geometry, the only one to obtain an exact expression for the Kerr-rotation and Kerr-ellipticity in the case of normal incidence. For all other cases, the final results as stated in **[Oppeneer, 2000]** will be given.

2.2.2.1 Complex Kerr angle in polar MOKE

For the P-MOKE geometry, the magnetization vector lies in plane of incidence and perpendicular to the surface, as shown in figure 2.6. The dielectric tensor is

$$\varepsilon(\omega) = \begin{pmatrix} \varepsilon & \varepsilon_{xy} & 0 \\ -\varepsilon_{xy} & \varepsilon & 0 \\ 0 & 0 & \varepsilon \end{pmatrix} \qquad 2.14$$

With $\varepsilon_{xy} \ll \varepsilon_{xx}$. The Fresnel-equation yields the refractive index n in the magnetic medium:

$$n_{\pm} = \sqrt{\varepsilon \pm i\varepsilon_{xy}} \qquad 2.15$$

The corresponding Eigen modes for the electric field in the medium are right- and left-circularly polarized waves. If normal incidence from vacuum is assumed, the Fresnel coefficients of reflection for circularly polarized light are given by:

$$r_{\pm} = \frac{n_{\pm}\text{-}1}{n_{\pm}+1} \qquad 2.16$$

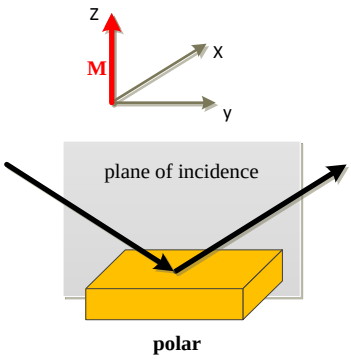

Figure 2.6: Polar MOKE. The magnetization is perpendicular to the surface and parallel to the plane of incidence.

Generally, the reflected wave is elliptically polarized, and the transformation from the incident to the reflected waves can use the reflection matrix:

$$\vec{E}^{(R)} = \begin{pmatrix} r_+ & 0 \\ 0 & r_- \end{pmatrix} \vec{E}^{(I)} \qquad 2.17$$

Because ε_{xy} is nonzero in equation 2.13, the reflected light is elliptically polarized, with the polarization plane tilted a small angle from the incident polarization. The ratio of the two reflected complex amplitudes can be calculated:

$$\frac{E_+}{E_-} = \frac{|E_+|}{|E_-|} e^{\Theta r\text{-}\Theta_I} = \frac{n_+\text{-}1 n_-\text{-}1}{n_+ + 1 n_- + 1} \qquad 2.18$$

The Kerr-Rotation angle can be determined:

$$\Theta_K = \frac{1}{2}\left(\Theta_r\text{-}\Theta_I\right) \qquad 2.19$$

The Kerr-ellipticity can be obtained from **[Oppeneer, 2000]**

$$\tan\varepsilon_K = \frac{|E_+|\text{-}|E_-|}{|E_+|\text{-}|E_-|} \qquad 2.20$$

For arbitrary incidence and using Cartesian coordinates, equation 2.15 can be rewritten as

$$\vec{E}^{(R)} = \tilde{A}^{-1} \begin{pmatrix} r_+ & 0 \\ 0 & r_- \end{pmatrix} \tilde{A} \qquad 2.21$$

Where $\tilde{A}$ is the transformation matrix from Cartesian to polar coordinates. The new reflection matrix can take the form

$$\hat{R} = \begin{pmatrix} r_{ss} & r_{sp} \\ r_{ps} & r_{pp} \end{pmatrix} \qquad 2.22$$

The Fresnel-coefficients for reflection (for arbitrary incidence) can be calculated from **[Oppeneer, 2000]**:

$$r_{ss} = \frac{n_0 \cos\phi_I - \bar{n}\cos\phi_T}{n_0 \cos\phi_I + \bar{n}\cos\phi_T} \qquad 2.23$$

$$r_{pp} = \frac{\bar{n}\cos\phi_I - n_0\cos\phi_T}{\bar{n}\cos\phi_I + n_0\cos\phi_T} \qquad 2.24$$

$$r_{sp} = r_{sp} = \frac{-n_0(n_+ - n_-)\cos\phi_I}{(n_0\cos\phi_I + \bar{n}\cos\phi_T)(\bar{n}\cos\phi_I + n_0\cos\phi_T)\cos\phi_T} \qquad 2.25$$

The cross-mode reflection coefficient $\mathbf{r_{sp}}$ couples the incident s-polarized to the reflected polarized wave, and $\mathbf{r_{ps}}$ the other way around. The Voigt parameter **Q** can be introduced to rewrite the equation in terms of $\mathbf{r_{sp}}$ only, which is valid to first order in **Q**. Together with $n_+ - n_- = \bar{n}\, Q \cos\phi_T$, the complex Kerr-angle for P-MOKE at oblique incidence can be written as:

$$\Theta_K^{(s)} + i\varepsilon_K^{(s)} = \frac{r_{ps}}{r_{ss}} = -\frac{i n_0 \bar{n} Q}{\bar{n}^2 - n_0^2} \frac{\cos\phi_I}{\cos(\phi_I - \phi_T)} \qquad 2.26$$

$$\Theta_K^{(p)} + i\varepsilon_K^{(p)} = \frac{r_{sp}}{r_{pp}} = -\frac{i n_0 \bar{n} Q}{\bar{n}^2 - n_0^2} \frac{\cos\phi_I}{\cos(\phi_I + \phi_T)} \qquad 2.27$$

2.2.2.2 Complex Kerr angle in the longitudinal MOKE

For the L-MOKE geometry, the magnetization vector is in plane of incidence and lies parallel to the surface, as shown in figure 2.7.

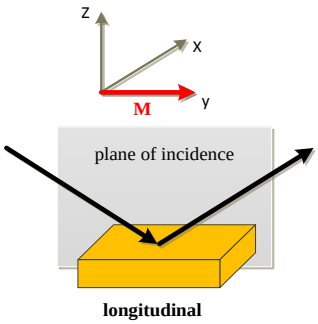

Figure 2.7: Longitudinal MOKE. The magnetization is parallel to the surface and the plane of incidence.

If the surface normal is chosen parallel to the z-axis, the dielectric tensor is:

$$\varepsilon(\omega) = \begin{pmatrix} \varepsilon & 0 & 0 \\ 0 & \varepsilon & \varepsilon_{yz} \\ 0 & \varepsilon_{yz} & \varepsilon \end{pmatrix} \qquad 2.28$$

The refractive index, is (up to the first order in ε_{yz}):

$$n_{\pm} = \sqrt{\varepsilon \pm i\varepsilon_{yz} \sin \phi_T^{\pm}} \qquad 2.29$$

Here, $\phi_T^{\pm}$ are the angles of refraction for the right- and left circularly polarized beams. With $n_+ - n_- = \bar{n}Q \sin \phi_T$ and $Q = i\varepsilon_{yz}/\varepsilon$, the complex Kerr-angle can be calculated according to **[Oppeneer, 2000]**:

$$\Theta_K^{(s)} + i\varepsilon_K^{(s)} = \frac{r_{ps}}{r_{ss}} \approx \frac{-in_0\bar{n}Q}{\bar{n}^2 - n_0^2} \frac{\cos\phi_I tan\phi_T}{\cos(\phi_I - \phi_T)} \qquad 2.30$$

$$\Theta_K^{(p)} + i\varepsilon_K^{(p)} = \frac{r_{sp}}{r_{pp}} = \frac{-in_0\bar{n}Q}{\bar{n}^2 - n_0^2} \frac{\cos\phi_I tan\phi_T}{\cos(\phi_I + \phi_T)} \qquad 2.31$$

2.2.2.3 Complex Kerr angle in the transversal MOKE

In the T-MOKE geometry, the magnetization vector is perpendicular to the plane of incidence and parallel to the surface, as shown in figure 2.8.

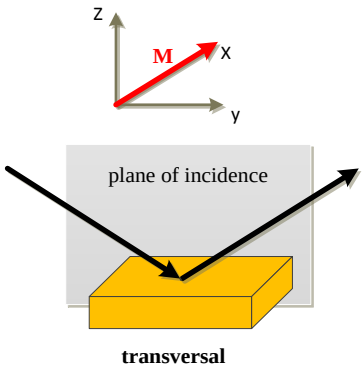

Figure 2.8: Transversal MOKE. The magnetization is parallel to the surface and perpendicular to the plane of incidence.

The dielectric tensor reads

$$\varepsilon(\omega) = \begin{pmatrix} \varepsilon & 0 & \varepsilon_{xz} \\ 0 & \varepsilon & 0 \\ -\varepsilon_{xz} & 0 & \varepsilon \end{pmatrix} \qquad 2.32$$

In the T-MOKE, a rotation is not observed, but the modulation of the intensity of the reflected light and it depends on the magnetization. The refractive indices for s- and p-polarized waves are:

$$n_s^2 = \varepsilon \qquad 2.33$$

$$n_p^2 = \varepsilon + \frac{\varepsilon_{xz}^2}{\varepsilon} \qquad 2.34$$

There is no coupling from s- to p-polarized light, and consequently there is no T-MOKE effect for s-polarized incident light.

Depending on the orientation of the in-plane magnetization of the sample ($\vec{M}_{\pm}$) the reflection coefficient for p-polarized light is:

$$r_{pp}(\vec{M}_{\pm}) \approx \bar{r}_{pp}\left(1 \pm \frac{\varepsilon_0 \varepsilon_{xz} sin2\phi_I}{\varepsilon^2 cos^2\,\phi_I - \varepsilon_0 \varepsilon - \varepsilon_0^2 sin^2\phi_I}\right) \qquad 2.33$$

Here, $\bar{r}_{pp}$ is the p-mode reflection coefficient for the magnetized material and ε_0 the dielectric constant of the incident medium.

2.3 Ultrafast Laser Induced Magnetization Dynamics

The demagnetization of thin films using a strong laser pulse was first observed by the group of Beaurepaire **[Beaurepaire et al, 1996]** , and since then it became an important tool in magnetization dynamics. They used the pump- probe MOKE with pulse duration of 60 fs. Their key results reproduced in figure 2.9 show that after the excitation pulse arrival, the Nickel magnetization drops to almost half of the equilibrium value in 2 ps, and then recovers slowly within hundreds of picoseconds.

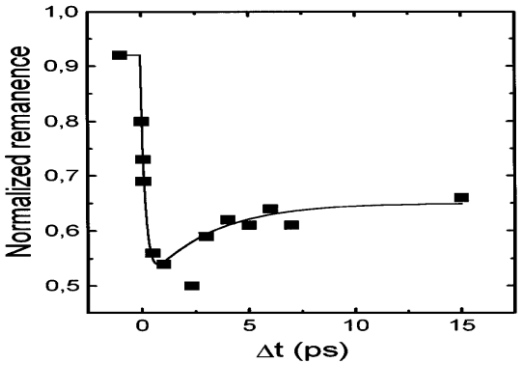

Figure 2.9: Time-resolved MOKE signal of a Ni film for 7 mJ/cm^2 pump fluence. The sample was excited by a strong laser pulse at t = 0 [Beaurepaire et al, 1996].

To explain this result a phenomenological three temperature model (3TM) was employed, as sketched in figure 2.10. The model describes the energy flow between three different heat baths, which are assumed to be in internal equilibrium: the electrons with the temperature T_e, the lattice with the temperature T_l and the spins with the temperature T_s.

In the pump-probe experiments, initially the electrons sub-system is excited by the laser pulse. Then the energy is transferred to the spin and a lattice subsystem within characteristic timescales until the entire system is in equilibrium. *Beaurepaire et al*. introduced a system of differential equations:

$$C_e(T_e)\frac{\partial T_e}{\partial t} = -G_{el}(T_e - T_l) - G_{es}(T_e - T_s) + P(t), \qquad 2.34.a$$

$$C_s(T_s)\frac{\partial T_s}{\partial t} = -G_{es}(T_s - T_e) - G_{ls}(T_s - T_l), \qquad 2.34.b$$

$$C_l(T_l)\frac{\partial T_l}{\partial t} = -G_{el}(T_l - T_e) - G_{sl}(T_l - T_s), \qquad 2.35.c$$

Where P(t) is the initial excitation from the laser, Cs, C_e and C_l are the heat capacities of the three systems and the Gs are the coupling constants between the capacities.

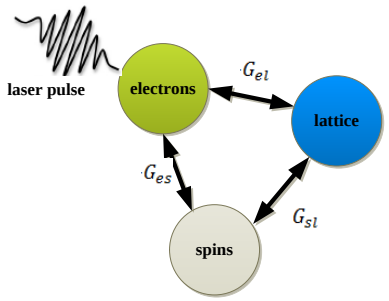

Figure 2.10: Energy distribution according to the three temperature model. The electron system is excited by the laser and then the energy is transferred to the lattice- and spin-systems.

The evolution of the three temperatures according to equation. 2.34 can be fitted to the experimental data by varying the coupling constants G as shown in figure 2.11.

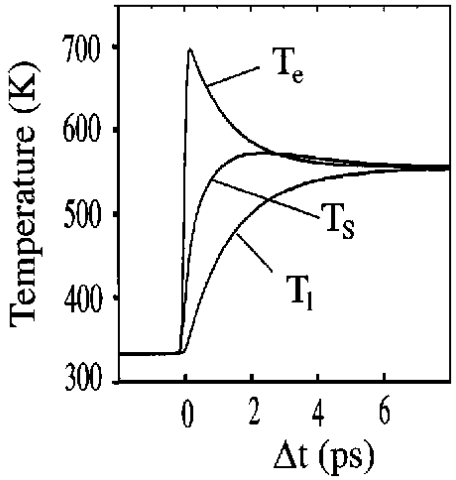

Figure 2.11: The temperatures of the three baths calculated using the three temperatures model with fitted interaction constants. (taken from [Beaurepaire et al, 1996]).

The model shows that the energy of the laser pulse is nearly instantly absorbed by the electron system. Then, the energy is redistributed to the spin and lattice subsystems. After around 2 ps, the exchange with the spin system is completed and 5 ps later all three baths reach equilibrium. The subsequent slow cooling is due to a heat transfer to the surrounding environment of the sample **[Beaurepaire et al, 1996]**.

Equation 2.34 is used to parameterize the demagnetization process and express the relevant time scales from the measured data. The main timescales we will use are: the demagnetization time τ_M, and recovery time τ_E.

Chapter 3 Experimental Techniques

The basic characteristics and details of the experimental setups are discussed. The first section will describe the preparation of samples by electron beam lithography. The second section will give an introduction to Magnetic Force Microscopy (MFM) that is used study magnetic domain of the samples. The third section deals with the static measurement setup, to characterize samples by recording magneto optical loops and to get preliminary information about the behavior of the samples. In the fourth section, the system used to measure the time response of the samples will be introduced.

3.1 Preparation of patterned Samples using Electron Beam Lithography

Electron-beam lithography (or **e-beam lithography**) is the practice of scanning a focused beam of electrons to draw custom shapes on a surface covered with an electron sensitive film called a resist ("exposing"). The electron beam changes the solubility of the resist enabling selective removal of either the exposed or non-exposed regions of the resist by immersing it in a solvent ("developing"). The purpose, as with photolithography, is to create very small structures in the resist that can subsequently be transferred to the substrate material, often by etching. e-beam lithography can be used to create patterns at the micro and Nanoscale **[Altissimoa, 2010]**.

The samples fabricated for this project are patterned microdots made of nickel (Ni) and cobalt Palladium ($Co_{65}Pd_{35}$) alloy. A schematic of electron beam lithography fabrication steps is shown in figure 3.1. A cleaned silicon substrate is spin coated with two layers of e-beam PMMA resist (Poly Methyl Meth Acrylate). With and immediate spin and oven bake (180^0C) applied to ensure even dispersion of the resist the two PMMA layers were applied according to the following specifications

1. PMMA 200K (e-beam resist AR-P-649.04): Recipe: C-RCP-4, 4000 rpm with pre acceleration; Thickness: ~150nm.
2. PMMA 950K (e-beam resist AR-P-679.02): Recipe: C-RCP-4, 4000 rpm with pre-acceleration; Thickness: ~70nm.

The desired structure (figure 3.2) was then drawn on the coated substrate using e-beam lithography: An electron beam was focused on the desired area using magnetic lenses. The direction of the electron beam was controlled by an electrostatic field produced by a set of deflection plates. The electron beam engraved structure on the resist. The exposed RMMA area was then removed by the e-beam fast developer AR600-55. Next, the $Co_{65}Pd_{35}$ alloy was deposited on the patterned substrate by Molecular Beam Epitaxy (MBE). Finally, the sample was immersed in Aceton and Propanol to remove the resist mask and obtain the desired structure. This process is called the lift-off **[Tseng et al, 2003]**.

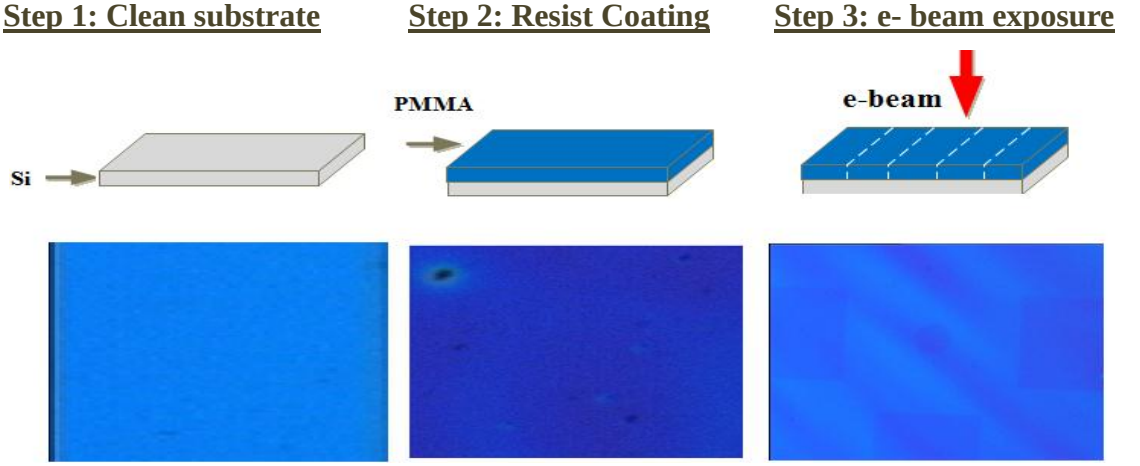

Silicon (Si) substrate after cleaning. **Sample after e-beam resists (PMMA) coating.** **The sample structure after e-beam exposure.**

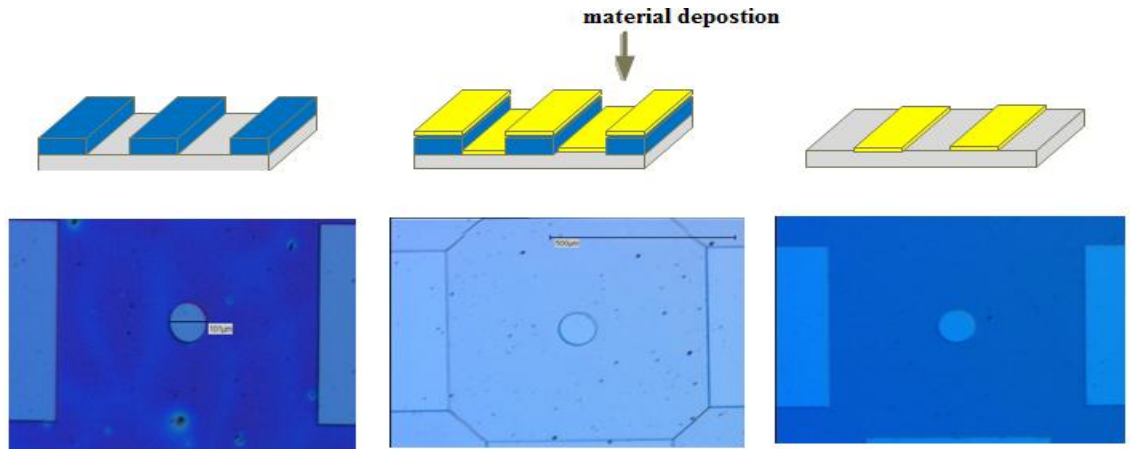

The sample structure after development by e-beam developer. **The sample structure after metallization by *molecular beam Epitaxy.*** **The sample structure after lift-off by Aceton and Propanol.**

Figure 3.1: Schematic diagram of the e-beam lithography steps (1 - 6).

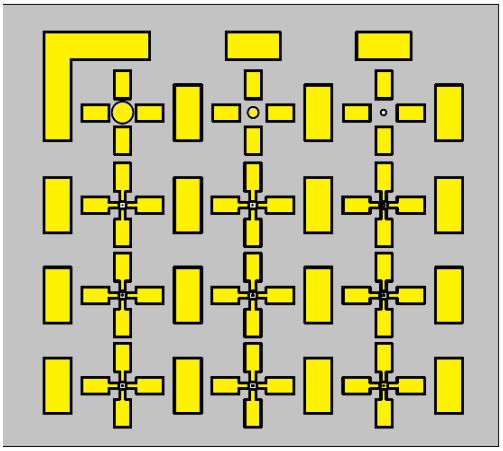

Figure 3.2: The desired structure of a sample. It consists of small circuit dots (500µm - 10µm diameter) surrounded by rectangular marks.

3.2 Magnetic Force Microscopy (MFM)

Magnetic Force Microscopy (MFM) was introduced shortly after the invention of the Atomic Force Microscope (AFM), and offered high resolution imaging of structures in superconductors, domain structures in hard and soft magnetic materials and found significant use for imaging and writing recording media **[Abelmann, 2005]**.

3.2.1 MFM principle

The principle is shown in Figure 3.3(b). The sample is mounted on a piezo-scanner, which provides spatial movement of the specimen along the three coordinate axes. Usually, the piezo-scanner is a thin-walled tube made of piezo-ceramics coated with a system of metal electrodes. In MFM, a magnetically coated sharp tip with ferromagnetic thin film (CoCr or NiFe) is used and mounted on a cantilever spring. The tip is placed close to the sample surface (10-100 nm) and interacts with the stray field emanating from the domain structure of the sample. The magnetic force (F) acting on the tip causes a bending of the cantilever and a vertical movement of the tip. The laser beam is focused on the cantilever. When the cantilever feels any stray field changes, the angle of the reflected light changes. The reflected light is detected by a split photodiode, and recorded to produce an image. **[Yaminsky, Tishin, 1999]**.

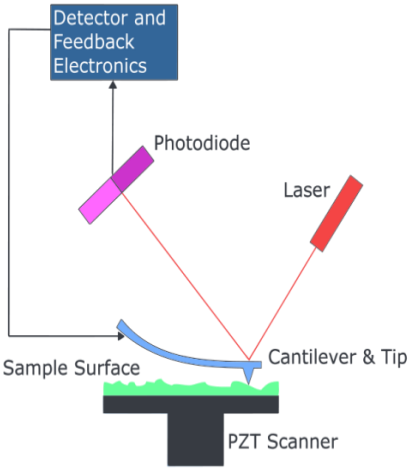

(a) **(b)**

Figure 3.3: (a) An MFM device. (b) MFM principle [Wikipedia, 2009].

3.2.2 MFM Operational Modes

MFM operates in static and dynamic modes. The static mode detects the magnetic force (F) acting on the tip. According to Hooke's law, the rising displacement Δz of the cantilever is measured (spring constant *k*).

$$F = -k\,\Delta z \qquad 3.1$$

The dynamic mode measures the force derivative dF/dz which is determined from a change in the dynamic properties of the cantilever, such as phase shifts, oscillation amplitude or resonance frequency. The cantilever is excited in a self-sustained to oscillate in its resonance frequency

$$f = f_0\sqrt{1 - \frac{\partial F|\partial z}{k}} \qquad 3.2$$

$$\Delta f = f - f_0 \approx -\frac{f_0}{2k}\frac{\partial Fz}{\partial z} \qquad 3.3$$

Where f_0 is the free resonance frequency of the cantilever with no tip-sample interaction. The approximation in equation (3.3) is valid when the change in the cantilever frequency is much smaller than the cantilever's resonance frequency, which is usually the case in MFM.

The above equations assume that the positive z direction points away from the sample, when the tip is attracted towards it. In such case the force is negative and the derivative is positive. Therefore, for attractive forces, the resonance frequency of the cantilever decreases and for repulsive forces the resonance frequency increases. The image is encoded in a way that attractive forces are depicted in dark color, while repulsive forces are coded bright color.

There are two ways to deal with resonance frequency measurement. For Amplitude Detection the cantilever oscillates at a frequency greater than the free resonance frequency, and that means changes in the resonance frequency cause deflections of the cantilever. In the Frequency Detection the cantilever vibrates at the resonance frequency *f* while the amplitude is controlled by the feedback loop.

In the 2-pass mode the MFM measurements are made by scanning the same line twice. In the first pass it uses the semi-contact (tapping) mode of operation, where the surface topography is recorded to be used for the second pass (figure3.4). After the first pass, the cantilever is kept above the surface at the required height *dZ* and follows the same topographic contour. Because of the height *dZ*, the cantilever is only affected by long-ranged magnetic forces **[Hendrych et al, 2007]**.

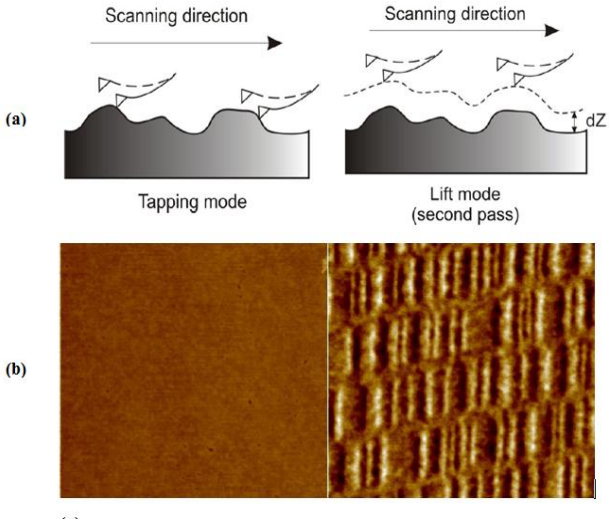

Figure 3.4: (a) Two passes methods for MFM. (b) Left image: a first pass: surface topography imaging-tapping mode (hard drive). Right image: a second pass: lift scan follows the topography to obtain magnetic contrast image (magnetic recording medium). [Hendrych et al, 2007].

3.3 Static MOKE Microscope Setup

A schematic of the setup is shown in figure 3.5. The light source is a laser diode with a wavelength of approximately 670 nm. The polarizer is installed after the light source to ensure that the light is linearly polarized. The polarized light is then effectively pulsed at about 600 Hz by an optical chopper. The sample is mounted between the poles of a Broker electromagnet, where an external magnetic field of more than H = 150mT can be applied in order to change the sample magnetization. In this set up, there are two possibilities for guiding the beam to the sample:

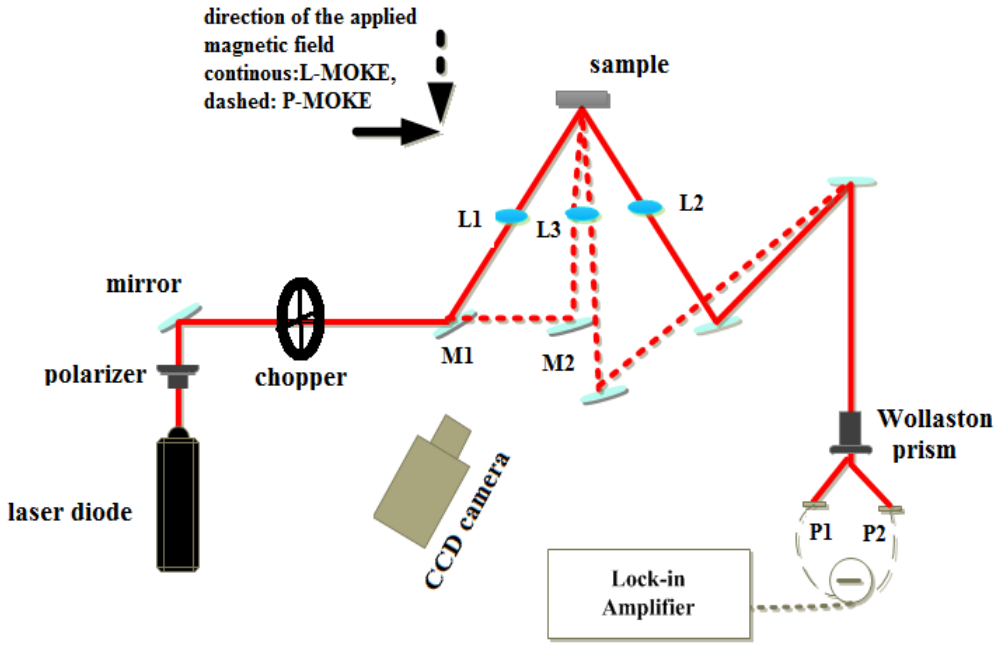

Figure 3.5: Schematic of static MOKE setup in longitudinal and polar configurations.

1- Longitudinal L-MOKE, continuous line in figure (3.5)

If mirror M1 is moved into the beam path, it deflects the laser beam by an angle of 45°. Afterwards, the beam is focussed to the sample using lens L1, reflected back from the surface, and collimated by lens L2. And by means of two mirrors, the beam can be aligned into the detector with a defined position. In this case, the magnetic field is set in the plane of the sample.

2- Polar P-MOKE, dashed line in figure (3.5)

If mirror M_1 is removed from the beam path, the laser beam moves straight and gets reflected by M2 at an almost a right angle with respect to the sample surface. The beam is focussed by lens L3 and, after reflection from the sample, it is collimated by L3. Afterwards, the beam is steered into the detector by two mirrors. In this case, the magnetic field is set perpendicular to the sample surface. The incoming and the outgoing laser beams have to be aligned through a hole in one of the pole shoes of the electromagnet.

A detector contains a birefringent crystal (Wollaston prism), which refracts the two perpendicular components of the electric field of the incoming laser beam in different directions **[Wikipedia, 2013]**. Afterwards, the two beams can be separately measured by two photodiodes (P1and P2) and the difference signal can be calculated. The signal from the photodiodes is then coupled with the measured frequency of the optical chopper through a lock-in amplifier.

The lock-in amplifier ignores all output from the photodiodes except the one with the same frequency as the optical chopper. In this manner, a signal that would otherwise be drowned out by noise becomes easier to observe **[Armen, 2008]**. The obtained normalized differential signal $(I_1-I_2)/(I_1+I_2)$ is directly proportional to the Kerr angle θ_{Kerr} **[Trudel et al, 2010]**.

3.4 Time-Resolved MOKE: General Setup

A magnetized system can temporarily be demagnetized by a strong laser pulse, where it is interesting to measure the rate of demagnetization and recovery. Since these effects are very fast, with the demagnetization reaching the sub-picosecond timescale, it is necessary to find a technique that can excite the sample, and measure the magnetization state within few femtoseconds before and after the excitation. For this purpose, the pump-probe has been developed.

3.4.1 The Laser Amplifier System

The laser amplifier system from (Mountain view, CA, USA), used in this setup contains four different parts, as shown in figure 3.6. This system has been designed for high pulse energy, short pulse duration and long-term stability.

The Millennia Pro is a Diode Pumped Solid State (DPSS) laser, pumped by a diode laser fiber at 1064 nm wavelength. The Millennia Pro has a optical X-cavity resonator where the active medium is neodymium yttrium vanadate ($NdYVO_4$). The frequency is doubled by lithium triborate (LBO) crystal to generate green beam with a continuous optical power of 4.3 W at 532 nm wavelength **[Spectra Physics, 2001]**.

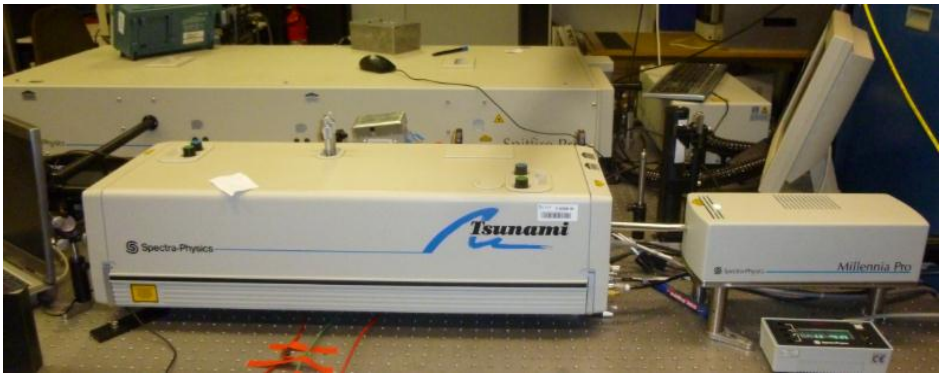

(a)

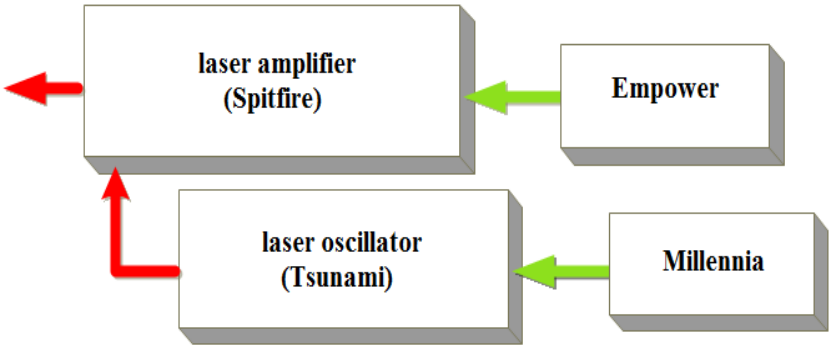

(b)

Figure 3.6: (a) laser amplifier systems (b) schematic of the laser amplifier system used in the time-resolved MOKE set up.

The Tsunami is a titanium-sapphire (Ti: Sa) based laser to create ultrafast pulses with a central wavelength of 800 nm. The active medium is a titanium-doped sapphire crystal that is pumped by CW green beam from Millennia Pro **[Spectra Physics 01, 2002]**. One of the key parameters that is defined by the oscillator is the spectral bandwidth. A high bandwidth is particularly important, because it is directly connected to the minimum pulse duration via the time-bandwidth product (TBP).

For Gaussian pulses, this relation is given by $\Delta\nu\Delta t \geq .441$ where $\Delta\nu$ is the frequency at full-width at half-maximum (FWHM) and Δt is the duration at half maximum **[Rullière, 2005]**. $\Delta\nu = \Delta\lambda \cdot (c / \lambda^2)$ can be used to convert wavelength to frequency bandwidth, if the bandwidth is small. Here, c is the speed of light in vacuum, λ is the central wavelength **[Paschotta, 2008]**. The Tsunami can provide a spectral bandwidth of around $\Delta\lambda$ = 60 nm. The repetition rate of the Tsunami is 80MHz and its average output power is around P_T = 460mW. The beam generated by the oscillator is then reflected into the Spitfire.

The Empower is a Q-switched, DPSS laser emits 527 nm waves with 1 kHz repetition rate. The active medium is Nd:YLF crystal that emits light at 1053 nm, which is frequency-doubled by an LBO crystal to a green beam at 527 nm wavelength. Q-switching is provided via acousto-optic modulators (AOM) which enables the production of high energy pulses with time durations of ~100ns and average power of 20W. The Empower output beam serves as a pump source for the Spitfire Pro laser system **[Spectra Physics 02, 2002]**.

The Spitfire Pro is a second Ti:Sa laser that amplifies the incoming beam by passing it several times through an active medium. It is made of three internal parts: grating stretcher, regenerative amplifier and grating compressor, as shown in Figure 3.7.

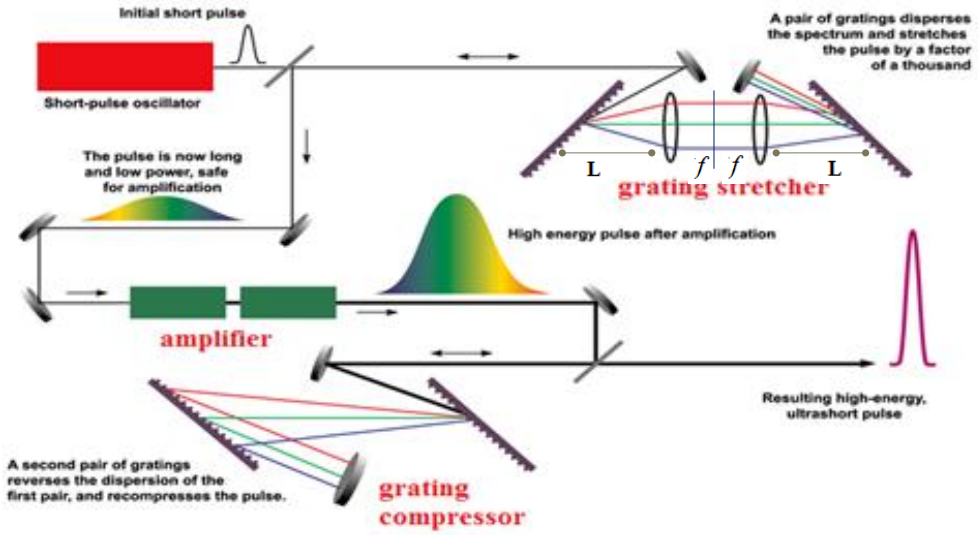

Figure 3.7: The Spitfire Pro system. It contains three internal parts: grating stretcher, regenerative amplifier and grating compressor.

The output pulse from the Tsunami is first temporally stretched by ***grating stretcher*** to increase the efficiency of amplification and to avoid damage of the Ti: Sa crystal in the Spitfire Pro. A grating-based stretcher consists of two anti-parallel gratings. To ensure that the beam returns parallel after passing the two gratings, two converging lenses with the same focal length *f* are placed between the gratings at a distance *2f* from each other. Since the pulse of longer wavelength (red) traverses a shorter distance compared to the pulse of shorter wavelength (blue) the spectral components are slightly shifted in time after they have left the stretcher. Consequently, the pulse is broadened **[Spectra Physics, 2005]**.

This pulse then enters the ***regenerative amplifier*** to be amplified in a Ti: Sapphire crystal that is pumped with the Empower beam. Two Pockels cell are used in order to select individual pulses from the train of stretched seed pulses and capture them in the regenerative amplifier. The input Pockels cell allows the pulse from the *Tsunami* to arrive at the Ti:sapphire crystal at the same time with the pump pulse from the Empower. The selected and stretched pulses then make multiple passes through the regenerative amplifier, increasing the energy. The output Pockels cell works in the amplifier cavity to release an amplified pulse at specific time.

Finally, the pulse duration of the amplified pulses needs to be shortened again. This is done by a ***grating compressor*** which acts in the reverse way of the grating stretcher; it uses different distances to move the spectral component. The Spitfire output has average power of more than 1 W at a repetition rate of 1 kHz **[Spectra Physics, 2005] [Vahaplar, 2011]**.

3.4.2 Description of the Beam Path

The output beam of the Spitfire Pro travels through several optical elements before they reach the sample. The complete beam path is shown in figure (3.8).

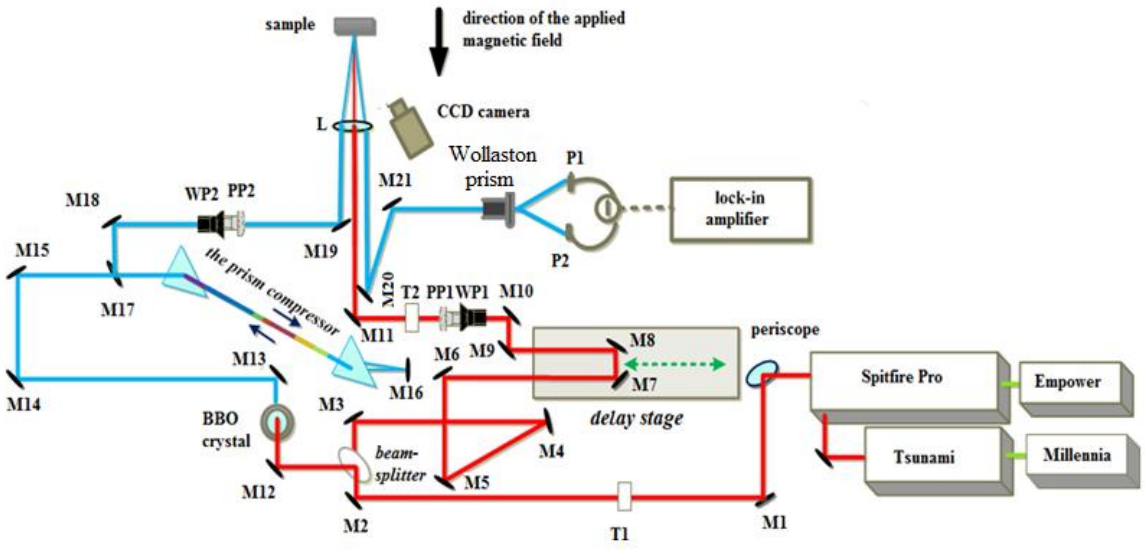

Figure 3.8: Beam path of the TR-MOKE setup in polar configuration.

The laser beam is first lowered to a certain height (12 cm) by a ***periscope***. The beam is reflected by it and a mirror (M1), and passed through the ***telescope*** T1 (two fused silicate lenses with foci of f_1 = 300mm and f_2 = -200mm) to reduce the spot size of the beam. Afterwards, the beam is split into two parts, a pump beam and probe beam, by ***the beam-splitter***. The two beam paths will be described separately for better understanding of what follows.

The pump beam path (red)

After passing from the beam-splitter, the pump-beam is reflected from several mirrors (M3, M4, and M5and M6) to two mirrors (M7 and M8) which are mounted on ***a delay stage***. By moving the stage, the path length of the pump-beam can varied with respect to the path length of the probe beam. Thus, a time-delay between the two beams in the femtosecond timescale can be adjusted. After the delay stage, the beam passes ***a half wave plate*** WP1 and ***a prism polarizer*** PP1 to adjust its polarization and power. It then passes the ***telescope*** T2 (similar to T1)**,** mirror M11 and lens L1, the pump-beam is focused onto the sample.

The probe beam path (blue)

After passing from the beam-splitter, the pump-beam is frequency-doubled to λ_c = 400 nm (blue) using ***a beta-barium borate crystal (BBO)*** crystal, and due to highly nonlinear optical effects, a second harmonic of the incident beam is produced. Using the mirrors

M13, M14 and M15, the probe beam is reflected into ***the prism compressor*** to regulate the duration of the probe beam and refract the remaining red beam out of the beam path.

Afterward, the beam is routed by mirrors M17 and M18 into the combination of wave plate WP2 and polarizer PP2 to adjust its polarization and power. Then, the beam is reflected to the sample at an almost right angle with respect to the sample surface. The lens L is used to get a parallel beam. By applying two mirrors M20 and M21, the probe beam is adjusted onto the ***photodiodes*** (P1 and P2) of the detector (similar to the Static MOKE setup).

3.4.3 Preparation of the time-resolved MOKE setup

3.4.3.1 Determination of the zero time-delay (t_0)

In this setup, a photodiode was mounted instead of the sample. Then, the pump and probe *beams* overlapped on a photodiode at the same signal, as shown in figure 3.9.

The zero-delay (x_0) is the position value when, the pump and probe beams arrive at the sample at exactly the same time. Figure 3.10(a), shows the normalized signal of the photodiode at different stage settings.

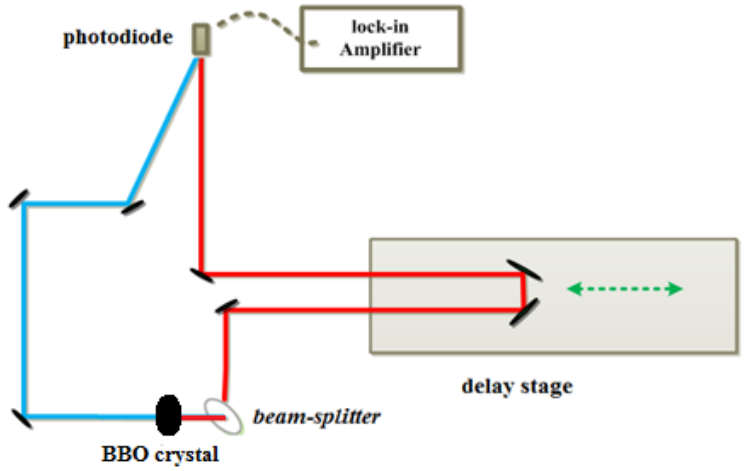

Figure 3.9: Overview of the 2 beams paths to find the zero delay.

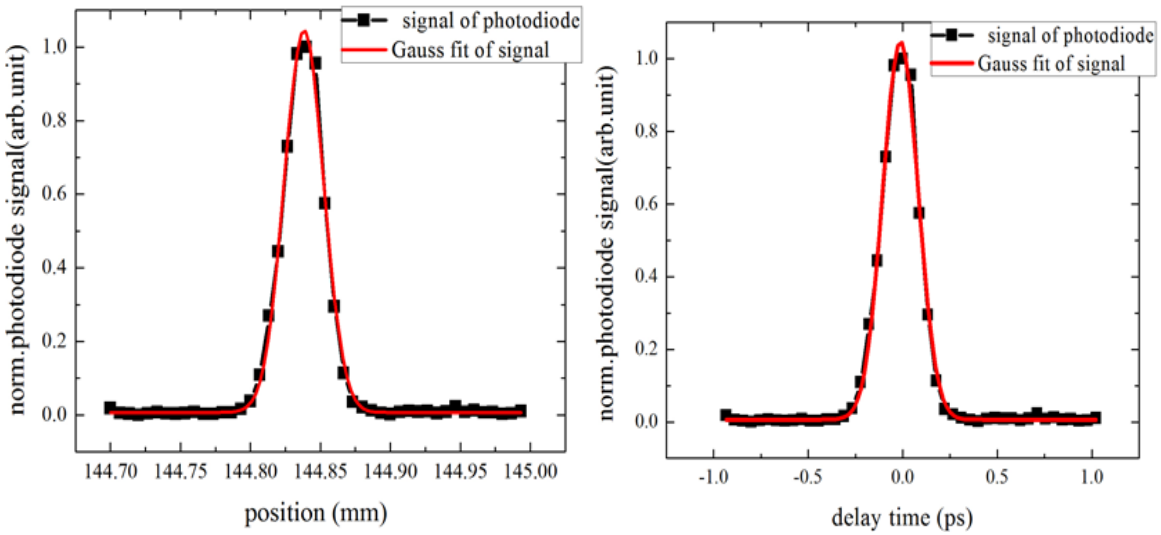

Figure 3.10: Normalized photodiode signal used to determine the zero delay. (a) The fitted Gaussian (red) yields the zero delay and (b) the delay time.

The obtained signal was sharp, with a narrow peak, and that allowed a good determination of the zero delay position. A Gaussian curve fit yielded that position at x_0 = 144.84mm. Using this value the delay time between the two beams, as shown in figure 3.10 (b), is calculated from $\Delta t = 2(x-x_0)/c$.

3.4.3.2 Pulse duration of the pump beam

Autocorrelation was used to measure the pulse duration of ultra fast lasers using the non-collinear second harmonic generation technique. The incoming beam was split into two identical pulses and overlapped spatially in the non-linear crystal. The intensity of the generated second harmonic wave depends on the temporal overlap of the two pulses. By scanning one of the pulses delay, the autocorrelation function was defined, and the pulse duration was calculated, assuming a Gaussian incoming pulse shape **[eKspla, 2011]**.

The pump beam pulse duration at FWHM was Δt = 80fs assuming a Gaussian profile. Figure 3.11 shows the autocorrelation of the pump beam.

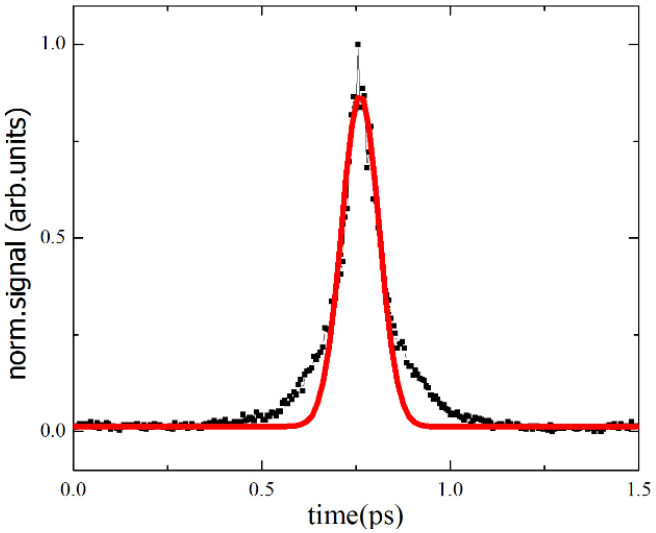

Figure 3.11: Autocorrelation of the pump beam with pulse duration of τ= 80fs.

Chapter 4 Measurements and Results

In this chapter the results and analysis will be presented. First, the magneto-optic Kerr-effect was employed to study the effect of thickness, size and ratio on the Ni magnetic behavior. Then the magnetic properties of $Co_{65}Pd_{35}$ were studied using MFM, SQUID, and MOKE magnetometer. The magneto-optic Kerr-effect was employed to study the magnetic dynamics in $Co_{65}Pd_{35}$ circular dot arrays. Finally, the ultrafast magnetization dynamics of $Co_{65}Pd_{35}$ and Ni_xPd_{100-x} films were studied by the time resolved magneto-optical Kerr effect. Table 4.1 shows the various samples constructed and their specifications and testing techniques used.

ID	Sample's Name	Form d (μm)	Composition	T (nm)	Substrate / capping material (t[nm])	Method of Preparation	Experimental Techniques
1	Nickel	Film	Ni_{100}	5	Si(40)/--	MBE	L-MOKE
2	Nickel	Film	Ni_{100}	10	Si(40)/--	MBE	L-MOKE
3	Nickel	Film	Ni_{100}	50	Si(40)/--	MBE	L-MOKE
4	Nickel	Film	Ni_{100}	5	Si(40)/Al(5)	MBE	L-MOKE
5	Nickel	Film	Ni_{100}	10	Si(40)/Al(5)	MBE	L-MOKE
6	Nickel	Film	Ni_{100}	50	Si(40)/Al(5)	MBE	L-MOKE
7	Nickel	Disk (d=10)	Ni_{100}	50	Si(40)/--	EBL& MBE	L-MOKE
8	Nickel	Disk (d=50)	Ni_{100}	50	Si(40)/--	EBL& MBE	L-MOKE
9	Nickel	Disk (d=100)	Ni_{100}	50	Si(40)/--	EBL& MBE	L-MOKE
10	Nickel	Disk (d=200)	Ni_{100}	50	Si(40)/--	EBL& MBE	L-MOKE
11	Nickel	Disk (d=500)	Ni_{100}	50	Si(40)/--	EBL& MBE	L-MOKE
12	Nickel Palladium	Film	$Ni_{90}Pd_{10}$	20	Si(20)/--	MBE	L-MOKE
13	Nickel Palladium	Film	$Ni_{80}Pd_{20}$	20	Si(20)/--	MBE	L-MOKE
14	Nickel Palladium	Film	$Ni_{70}Pd_{30}$	20	Si(20)/--	MBE	L-MOKE
15	Nickel Palladium	Film	$Ni_{65}Pd_{35}$	20	Si(20)/--	MBE	Tr-MOKE
16	Nickel Palladium	Film	$Ni_{60}Pd_{40}$	20	Si(20)/--	MBE	L-MOKE
17	Nickel Palladium	Film	$Ni_{55}Pd_{45}$	20	Si(20)/--	MBE	P-MOKE, Tr-MOKE
18	Nickel Palladium	Film	$Ni_{45}Pd_{10}$	20	Si(20)/--	MBE	P-MOKE, Tr-MOKE

19	**Nickel Palladium**	**Film**	**$Ni_{40}Pd_{60}$**	**20**	**Si(20)/--**	**MBE**	**P-MOKE**
20	**Nickel Palladium**	**Film**	**$Ni_{35}Pd_{65}$**	**20**	**Si(20)/--**	**MBE**	**Tr-MOKE**
21	**Cobalt Palladium**	**Film**	**$Co_{65}Pd_{35}$**	**40**	**Si(20)/--**	**MBE**	**MFM ,SQUID P-MOKE Tr-MOKE**
22	**Cobalt Palladium**	**Disk(d=50)**	**$Co_{65}Pd_{35}$**	**40**	**Si(20)/--**	**EBL& MBE**	**MFM, P-MOKE**
23	**Cobalt Palladium**	**circular dots arrays (d=5, s=5)**	**$Co_{65}Pd_{35}$**	**40**	**Si(20)/--**	**EBL& MBE**	**P-MOKE, Tr-MOKE**
24	**Cobalt Palladium**	**circular dots arrays (d=5, s=10)**	**$Co_{65}Pd_{35}$**	**40**	**Si(20nm)/--**	**EBL& MBE**	**P-MOKE, Tr-MOKE**

Table 4.1 List of samples made, their specifications and testing techniques used.

4.1 Magneto-Optic Kerr Effect Investigations of Nickel (Ni)

4.1.1 Preliminary results on pure Nickel

A first characterization of the samples was done employing the static MOKE microscope setup (longitudinal configuration) as described in section 3.2. Thereby, information on anisotropy, switching fields, coercively fields and saturation fields have been gained. For that objective the dependence of the magneto-optic signal on the magnetic field was recorded,resulting in hysteresis like loops. These loops do not directly reflect the magnetization of the sample, as the measured signal consists of magnetic and optical contributions. Therefore these loops will be addressed as magneto-optic loops.

A 50nm Ni film was used to calibrate the static MOKE microscope setup. This helps to confirm whether the setup can detect the Kerr effect or not. Figure 4.1 shows the average of 10 hysteresis loops (or magneto-optic loop) result for Ni film. It was measured in an in-plane configuration (L-MOKE). The loop reveals that the Ni film sample saturates at H ~ 6 mT. and coercivity field at ~5mT.

Figure 4.2 shows the loops for the Nickel sample at different angles (θ), of the external field. Relative to the sample surface normal. The samples were rotated around an axis parallel to the surface normal. Superimposed curves do not reveal considerable change between magnetization values for different angles.

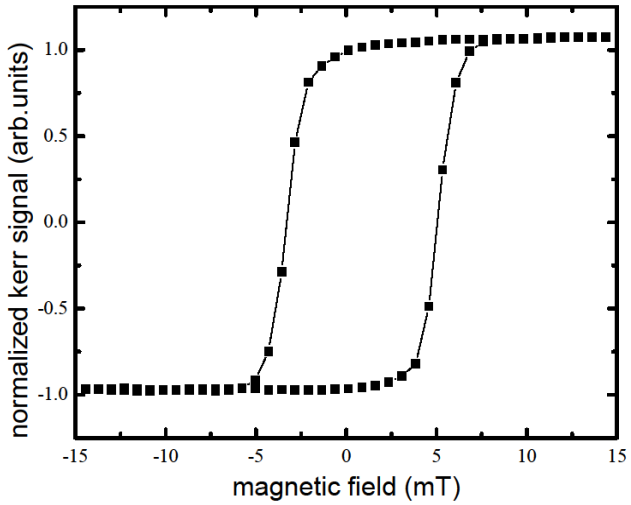

Figure 4.1: Hysteresis loop result of a 50 nm thick of Ni using static MOKE microscope setup in plane configuration (L-MOKE).

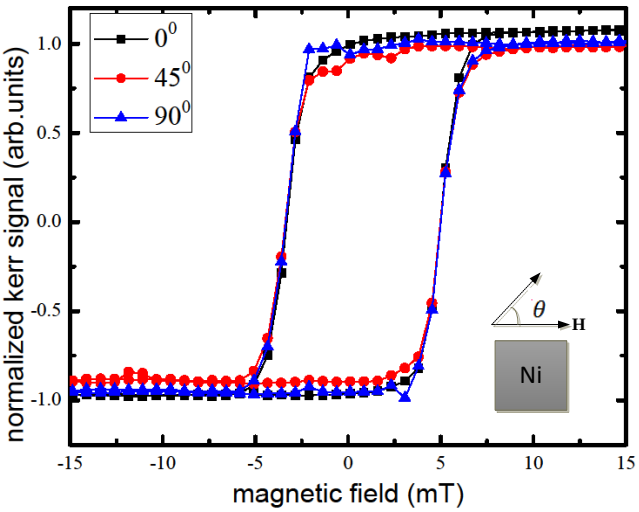

Figure 4.2: Hysteresis loops for a Nickel 50nm thin film measured at θ = 0^0, 45^0 and 90^0 with respect to the applied field.

A direct measurement of Kerr-rotation or Kerr-ellipticity was not possible using the Kerr effect. In addition, several adjustments were necessary after changing the samples. In that respect magnetization measurements cannot be compared before normalization.

4.1.2 Ni films with varying thickness

Thin films of Ni on Si substrates have been produced with thicknesses 5, 10 and 50nm. Other Ni films with a same thickness and with a 5 nm Aluminum (Al) capping layer were produced. Figure 4.3 shows the longitudinal MOKE loops of varying thin Ni film

thicknesses with and without a capping layer of 5nm Al. The loop became wider as the thickness increased. This is consistent with the magneto-static energy as the demagnetizing field decreases with increasing thickness and it requires less energy to have magnetic moments pointing out of the film plane.

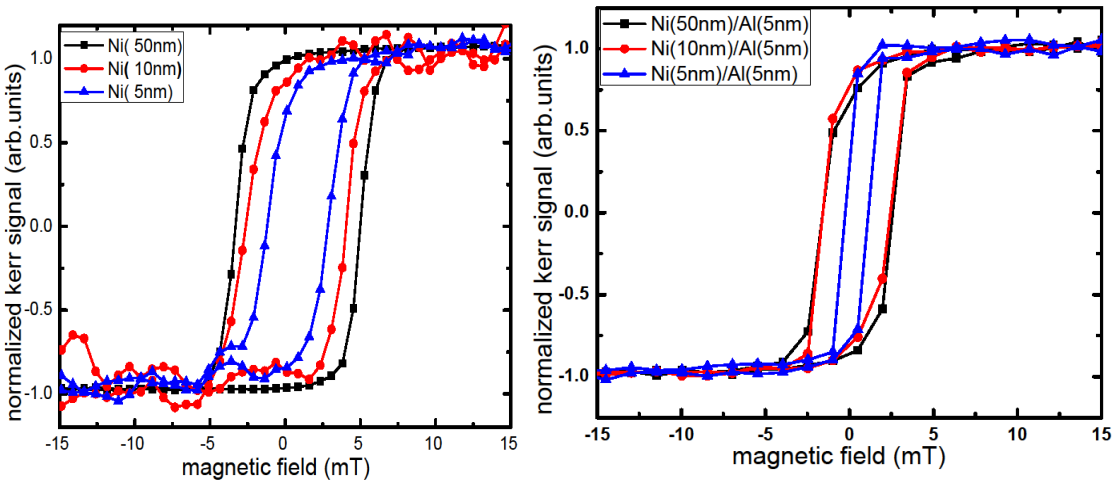

(a) (b)

Figure 4.3: The longitudinal MOKE loops for varying thin Ni film thicknesses (5,10 and 50 nm). (a) with and (b) without a capping layer of 5nm Al.

The coercivities magnetic fields for the samples are shown in Table 4.2. This data is plotted as functions of Ni film thickness in Figure 4.4. The coercivity of the Ni film with Al capping layer is smaller than the one without the capping layer. The coercivity increases with the Ni film thickness as expected since lower energy states are possible for systems with more magnetic moments up to some limit.

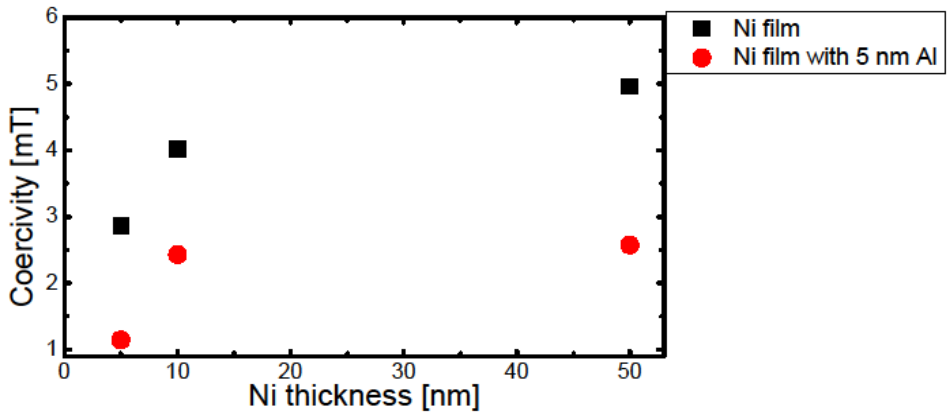

Figure 4.4: Coercivity magnetic field results for varying thin Ni film thicknesses with and without a capping layer of 5nm Al.

Ni thickness [nm]	5	10	50
Coercivity Si/Ni [mT]	2.863	4.016	4.954
Coercivity Si/Ni/Al [mT]	1.144	2.427	2.572

Table 4.2: Coercivity magnetic field results for varying thin Ni film thicknesses with and without a capping layer of 5 nm Al.

The coercive field H_c of the Ni film with Al capping layer is enough for the procees of data storage devices. In additional , this capping layer used as a protective layer to avoid the oxidation of Ni film , so it give a longer lifetime for Ni.

4.1.3 Ni disks with varying diameter

A series of circular Ni dots were fabricated using e-beam lithography onto Si substrates.

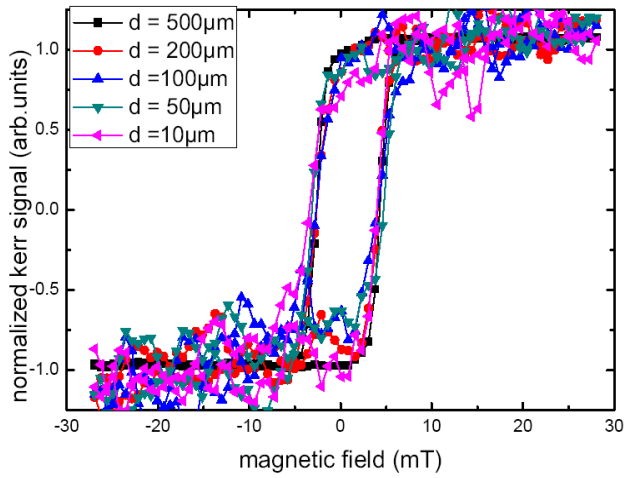

Figure 4.5: MOKE hysteresis loops of signal Ni dots with varing diameter from 10µm-500µm

The diameter (d) of the circular dots was varied from 10µm-500µm and the thickness of all dots was 50 nm. These loops were recorded with the coil providing a maximum field of 28 mT. Figure 4.5 shows that the diameter variation in this range does not have significant influence on the magnetic behavior of Ni.

4.1.4 Ni with varying ratio in Ni_xPd_{100-x} alloys

Metallic alloys composed of Ni_xPd_{100-x} ($45 \leq x \leq 100$) and 20nm thickness were produced. The samples with a nickel concentration of $> 55\%$ were measured in longitudinal geometry (see figure.4.6.a). And the samples with a nickel concentration of $\leq 55\%$ were measured in polar geometry (see figure.4.6.a) .As can be seen in both geometrics, the coercive field

increases with increasing Ni concentration, a similar trend can be observed for the saturation magnetic field.

Figure 4.7 shows the coercivity field H_c increases monotonically with Ni ratio. Since both the coercivity and saturation field increase with the Ni content, changes in coercivity could be due to variations in the magneto static energy.

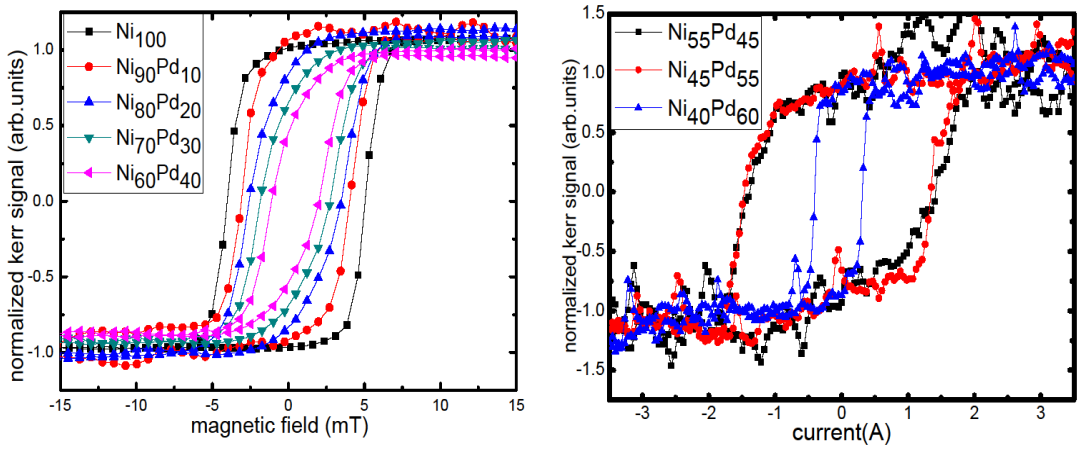

(a) **longitudinal geometry** (b) **polar geometry**

Figure 4.6: MOKE hysteresis loops of various Ni_xPd_{100-x} films for (a) longitudinal geometry and (b) polar geometry.

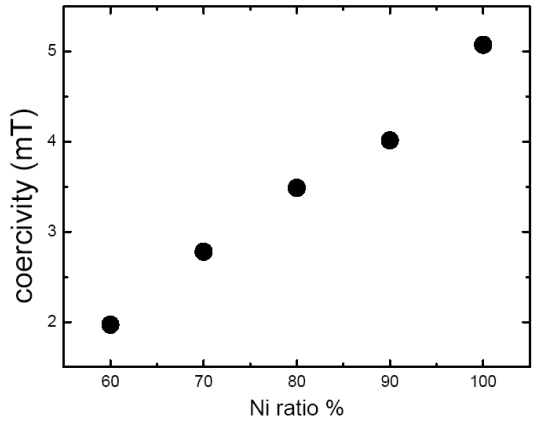

Figure 4.7: Dependence of the coercivity field (Hc) on the Ni_xPd_{x-1} films (L-MOKE geromitry).

4.2 Magnetic Properties of $Co_{65}Pd_{35}$

4.2.1 Magnetic domain of $Co_{65}Pd_{35}$

Figure 4.8(a-b) shows the magnetic domains in a thin $Co_{65}Pd_{35}$ flat film and a circular dot with 50µm diameter respectively as measured by Magnetic Force Microscopy (MFM**).** The

red areas or ‘up’ domains, point out of the plane of the page. The blue areas or ‘down’ domains point antiparallel to the up domains.

The net magnetization is the vector sum of all the magnetic domains in the sample, and can vary with an applied magnetic field (H). It will be zero, when the image has the same amount of up and down domains. Both samples show similar domain configurations with an average domain size of 80 nm for the flat film and 78 nm for the circular dot.

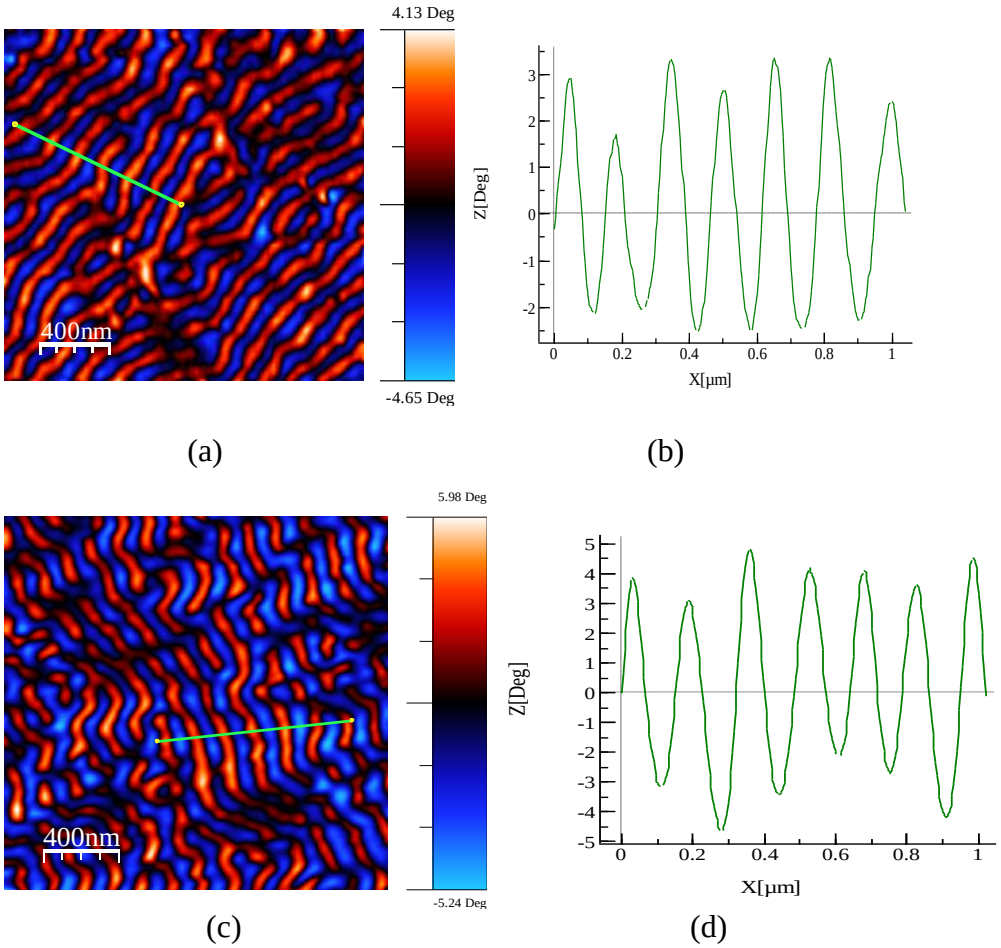

Figure 4.8: MFM images (a) $Co_{65}Pd_{35}$ flat film magnetic structure (b) Line section along the green line $Co_{65}Pd_{35}$ film image (domain size 80nm) (c) 50µm $Co_{65}Pd_{35}$ circuit dot magnetic structure (d) Line section along the green line of $Co_{65}Pd_{35}$ circuit dot image (domain size 78nm).

In these samples, the easy magnetization axis is out-of-plane. Therefore, all magnetic domains point perpendicular to the surface of the sample. In the static MOKE apparatus, the field is perpendicular to the sample surface (polar geometry).

4.2.2 SQUID measurements in $Co_{65}Pd_{35}$ film

For the SQUID measurement the whole magnetization of the sample can be measured, while MOKE measurements are more surface sensitive and yield more information from the topmost layers. In addition, in SQUID obsorved magnetic moment can be directly measured, while MOKE only allows the measurement of the relative magnetization with respect to the saturation magnetization. Figure 4.9 shows the hysteresis loop of $Co_{65}Pd_{35}$ (40nm). The sample saturates at an applied magnetic field of B_S = 3137 Oe, reaching a magnetic moment in saturation of M_S = 495 emu/cc.

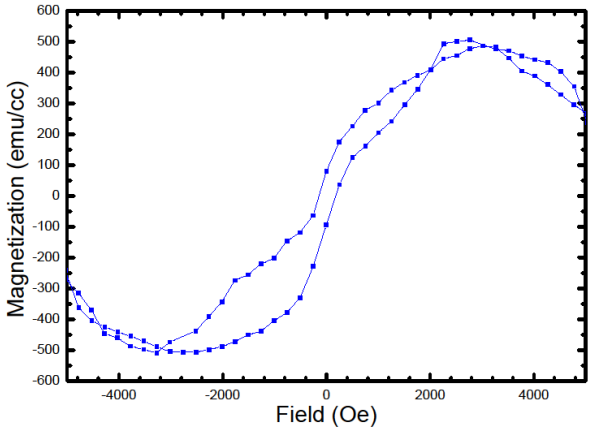

Figure 4.9: Hysteresis loop of $Co_{65}Pd_{35}$ film (40nm) by SQUID magnetometer.

4.2.3 MOKE investigations of $Co_{65}Pd_{35}$ circular dot arrays

Two structured samples were produced by optical lithography, as shown in figure 4.10. These samples consisted of arrays of circular dots with the same dot diameter (5 µm) and different inter-dot spacing (5 and 10 µm).

Figure 4.11 shows the polar magnetic Kerr hysteresis loops of the continuous $Co_{65}Pd_{35}$ film and isolated dot with 50µm diameter (figure.4.11.a) and $Co_{65}Pd_{35}$ circular dot with 5µm diameter at the central region of the patterned arrays with inter-dot separations of 5µm (figure.4.11.b) and 10µm (figure.4.11.c). The figure does not show significant change in the shape of all the hysteresis loops. The coercivity changes little between $Co_{65}Pd_{35}$ film and the isolated dot.

The significant change in coercivity H_c and saturation H_s are more interesting since these values are smaller in the continuous film but have increased upon the patterning (see table

4.3). In the patterned arrays, H_s changed from 200 to 300 mT. The separation to square edge ratio *s* /*a*, doubled from 1 to 2.

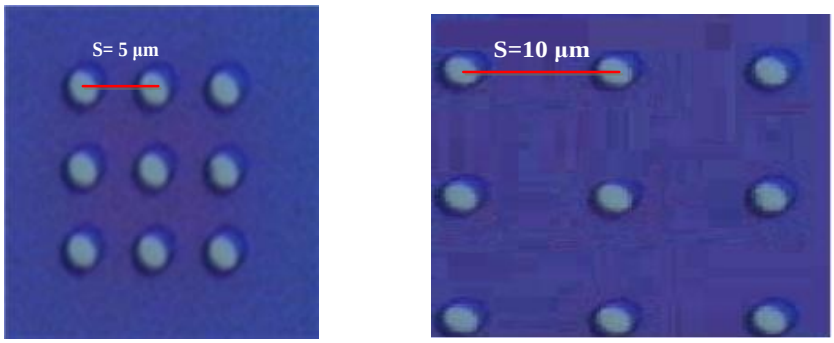

(a) (b)

Figure 4.10: Microscope images of the patterned arrays. The lateral diameter of the circular dot elements is 5 µm with the separation spacing of (a) 5µm (a) and (b) 10 µm.

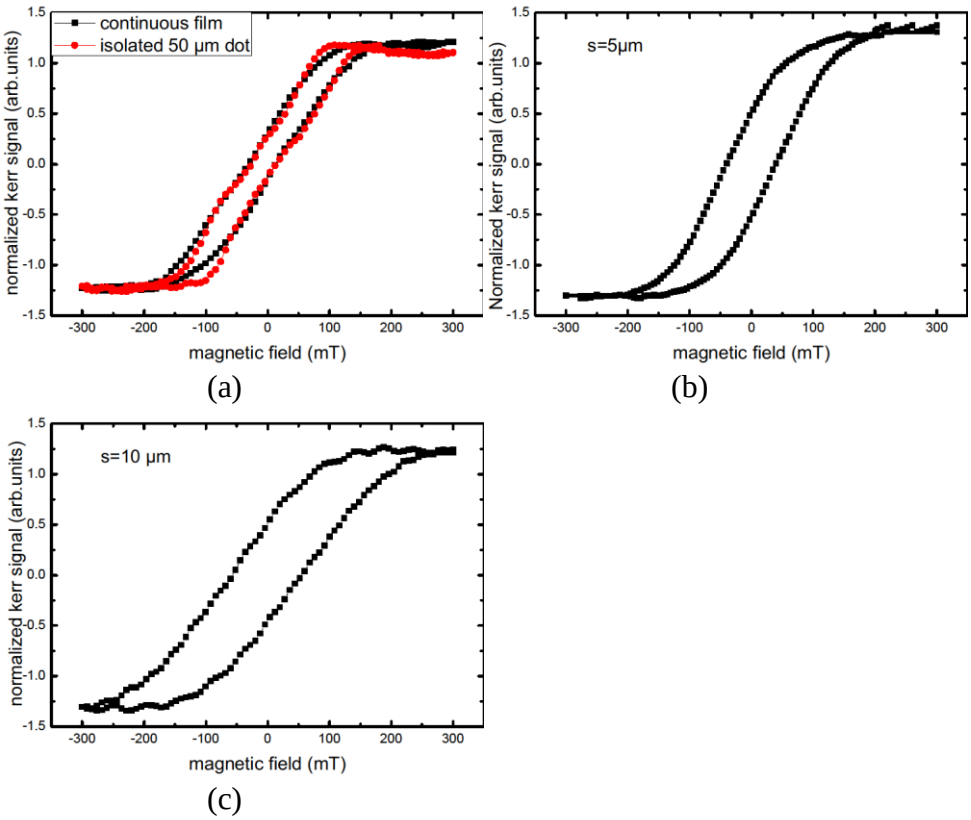

(a) (b)

(c)

Figure 4.11: The polar magnetic Kerr hysteresis loops of (a) the continuous $Co_{65}Pd_{35}$ film. Patterned arrays with 5µm dot diameter and separations of (a) 5 µm and (c) 10 µm.

Sample	Coercivity H_c (mT)	Saturation H_s (mT)
Continuous $Co_{65}Pd_{35}$ film	**31.3**	**171**
Isolated dot with d=50µm	**29.8**	**170.4**
$Co_{65}Pd_{35}$ arrays with s= 5µm	**40.5**	**203**
$Co_{65}Pd_{35}$ arrays with s= 10µm	**58.7**	**300.6**

Table 4.3: The coercivity H_c and saturation H_s of the continuous $Co_{65}Pd_{35}$ film and patterned arrays with 5µm dot diameter and separations of 5 and 10 µm.

The different values of *Hc* indicate the effect of inter-dot coupling on both the formation of single domain remnant state and also on the magnetization reversal process of dot arrays. This is similar to the enhanced coercivity observed in ultra thin epitaxial Fe dots **[Xu et al, 2001]** and in Fe square arrays **[Sun et al, 2011].**

4.3 Ultrafast Demagnetization of $Co_{65}Pd_{35}$ Film

4.3.1 Fitting and data extraction

The experimental setup presented in the previous chapter, allows the measurement of laser induced magnetization dynamics in thin films. A first step in understanding the demagnetization process is the measurement of the hysteresis loops at different times before and after the arrival of the pump beam t_0, as shown in figure 4.12. Both saturation and remanence magnetizations decreased within one pico second after t_0. After almost 25 ps, it has not even reached the original loop (see orange loop).(Original loop is black)

To determine the demagnetization time τ_M it is not necessary to record the complete hysteresis loop, because its shape is not changing (see figure 4.12).

It will be easer to see the changes if we can measure only one parameter for each time delay. Consequently, we traced the Kerr signal against the position of the delay stage at a pre set magnetic field enough to saturate the sample. Then, the magnetic field polarity is switched and the measurement is repeated.

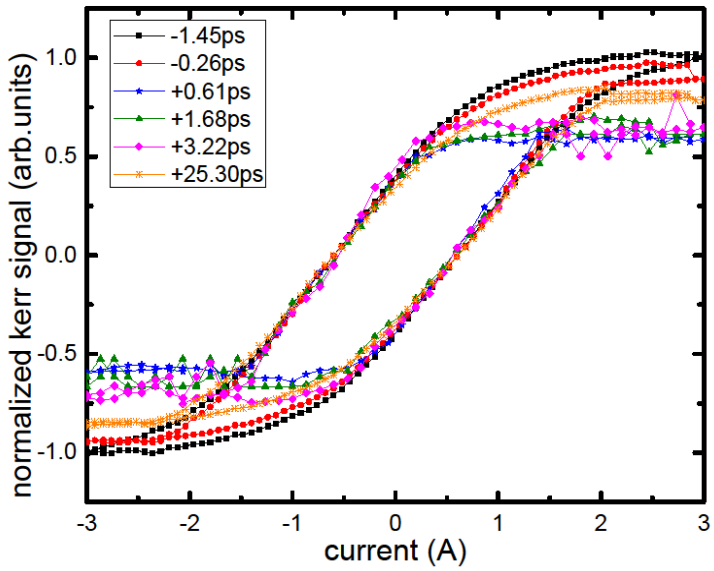

Figure 4.12: Hysteresis loop measured at different time delays between pump-and probe-beam. The pump-beam arrives around t = 0 ps. Afterwards, the saturation magnetization and the remanence of the sample drop rapidly (less than a picoseconds).

In figure 4.13, the Kerr signal for both fields is plotted against the time shift between the pump and probe beams. Figure 4.14 (black circuits) shows normalized difference signal between the two signals.

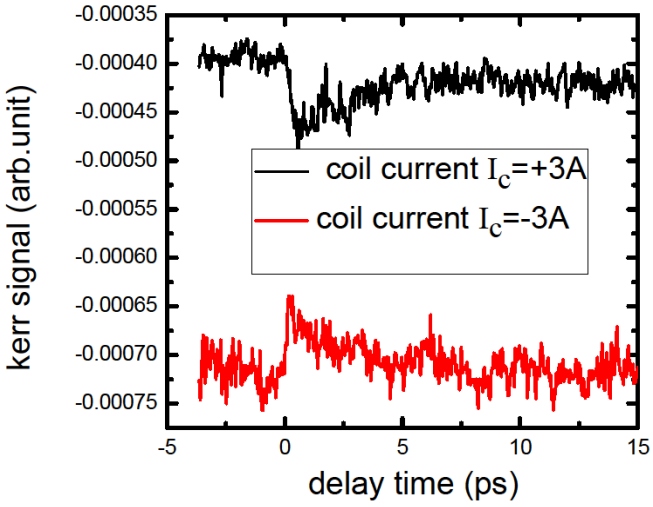

Figure 4.13: Demagnetization curves recorded for each direction of the magnetic field for $Co_{65}Pd_{35}$ (40nm).

In order to retrieve the characteristic time constants for the demagnetization time τ_M and recovery time τ_E the double exponential function is used to fit the curve

$$f(t) = A_0 - \left(A_1 . \left(1 - e^{-\frac{t-t_{Off}}{\tau_M}} \right) . e^{-\frac{t-t_{Off}}{\tau_E}} \right) . H(t-t_{Off}) \qquad (4.1)$$

Here, τ_{off} is the offset of the pump-beam arrival time relative to t = 0. $H(t-\tau_{Off})$ denotes a Heaviside function; A_0 and A_1 are fitting constants **[Radu et al, 2009].**

Figure (4.14) shows a fit of this function to the normalized difference signal of fig 4.13. The best fit for the demagnetization time was τ_M = 142 ± 13fs and the recovery time τ_E = 2.1 ± 0.14ps.

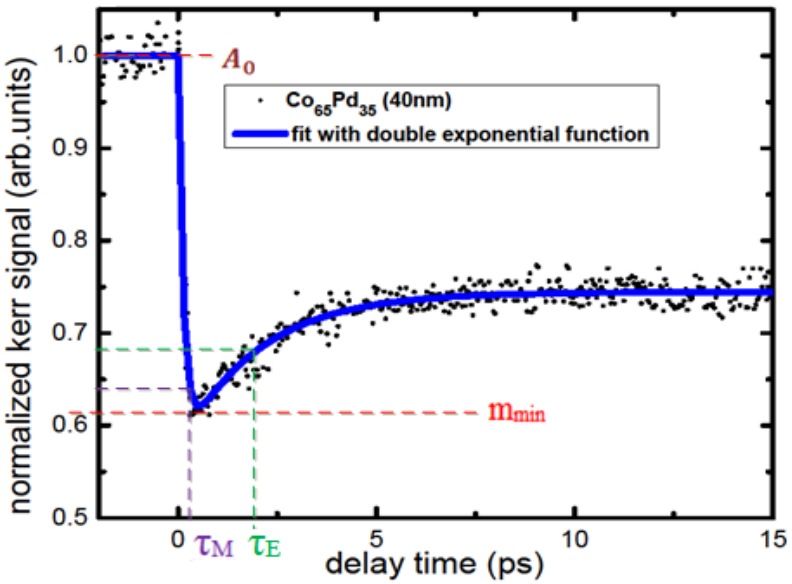

Figure 4.14: Demagnetization curve of a $Co_{65}Pd_{35}$ thin film fit with double-exponential function to determine the demagnetization time with added parameters.

Considering that A_0 corresponds to the magnetization m_0 before excitation, Here, for this measurement a minimum of 62% of the magnetization was reached after excitation (m_{min}=0.62). The quenching of the magnetization ($q = 1-m_{min}/m_0$) can be calculated **[Koopmans et al, 2010].**

4.3.2 Dependence of the demagnetization time on the excitation fluences

As noted in the previous section, the demagnetization can be determined by measuring a hysteresis loop at the time delay that corresponds to the peak signal in the curve of demagnetization. Figure 4.15 shows three polar MOKE hysteresis loops from a $Co_{65}Pd_{35}$ thin film, one made in the absence of a pump-beam (black hysteresis loop), and two

following excitation by a pump-beam (blue hysteresis loop) and more excitation fluence pump-beam (red hysteresis loop). The height of the hysteresis loop (saturation magnetization as well as remanence) decreases with increase fluence, due to demagnetization of the film. Figure 4.16 presents a selection of demagnetization curves measured at several different excitation fluences (3.18-6.50mJ/cm^2). The measurements were performed at room temperature in polar Kerr geometry. Clearly, the quenching of the magnetization (q) is stronger for higher pump fluences. Additionally, the recovery time τ_E and the demagnetization time τ_M get longer with increased pump fluence.

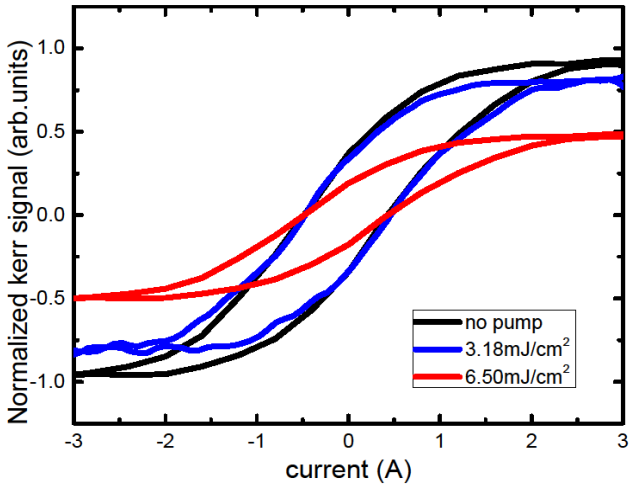

Figure 4.15: Polar MOKE hysteresis loops measured for $Co_{65}Pd_{35}$ thin film, with varied pump-beam fluences at the time delay corresponding to the peak of demagnetization curve.

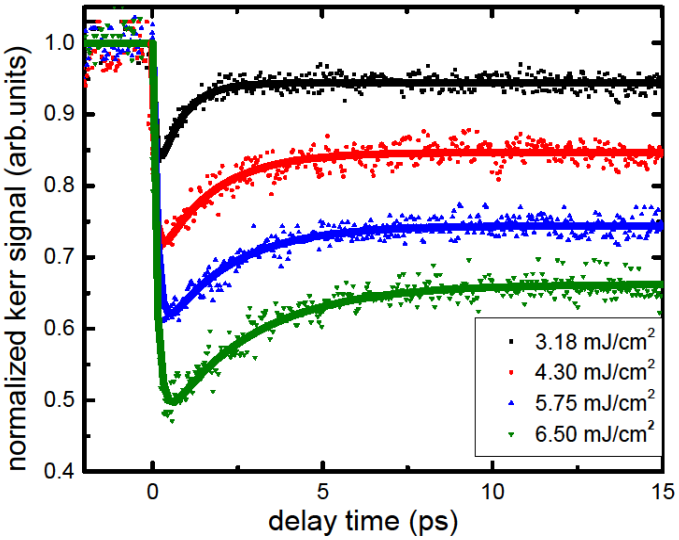

Figure 4.16: Demagnetization curve for a $Co_{65}Pd_{35}$ (40nm) thin film at different excitation fluences (3.18-6.50mJ/cm^2). The quenching and the recovery times become longer and the demagnetization becomes slower with increased pump fluences.

The results are presented in Table 4.4 for direct comparison. Using double-exponential fit, τ_M still shows slowing down, whereas the first recovery time τ_E shows a non-monotone behavior around 1 ps. The τ_M estimate is quite robust in comparison to the recovery time. This fact should be taken into account when comparing different models or experiments. As can be seen τ_M increase range is 118 -183 fs for quenching range of 0.16 - 0.51. This trend is similar to what has been previously reported for transition metals, thin films, for example, in Co-based materials **[Koopmans et al, 2010].**

Figure 4.17 show a comparison between Koopmans .et.al study and our results. In that study demagnetization time τ_M range is 150-300 fs for quenching range of 0.15 - 0.5. The difference in demagnetization time range compared to our data for $Co_{65}Pd_{35}$ could be due to the presence of Pd in the sample.

Fluences (mJ/cm^2)	**τ_M (fs)**	**τ_E (ps)**	**q(-)**
3.18	**118±15**	**0.7± 0.02**	**0.16**
4.30	**132 ±15**	**1.5± 0.03**	**0.28**
5.75	**142 ± 13**	**2.1± 0.14**	**0.39**
6.50	**183 ± 11**	**2.7± 0.10**	**0.51**

Table 4.4: Direct comparison of the demagnetization times, magnetization recovery times, quenching from the double-exponential fit.

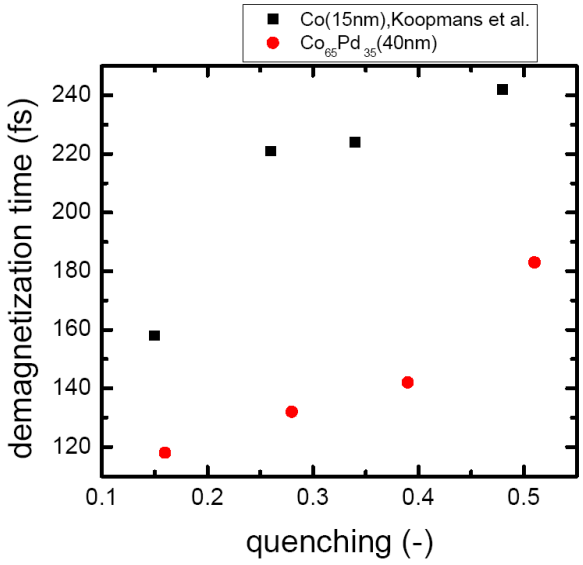

Figure 4.17: Demagnetization times reported for a 15 nm thin Co [Koopmans et al, 2010] compared to our measured demagnetization times for $Co_{65}Pd_{35}$ (40nm).

4.3.3 Ultrafast demagnetization of $Co_{65}Pd_{35}$ circular dots arrays

To compare the demagnetization times of the continuous $Co_{65}Pd_{35}$ film and patterned arrays with 5µm dot diameter and separations of 5 µm and 10 µm, the demagnetization curves of these arrays have been measured at the same fluence of pump-beam (4.30 mJ/cm^2.) with the magnetic field applied perpendicular to arrays, as shown in figure 4.18.

From the figure we see the quenching is stronger for s=10µm array compared to s =5µm array but the demagnetization times are 175 ps and 177ps respectively. Under the same fluence, the demagnetization time of the continues film is 142 ps for less quenching. This comparison is plotted in fig.4.19.

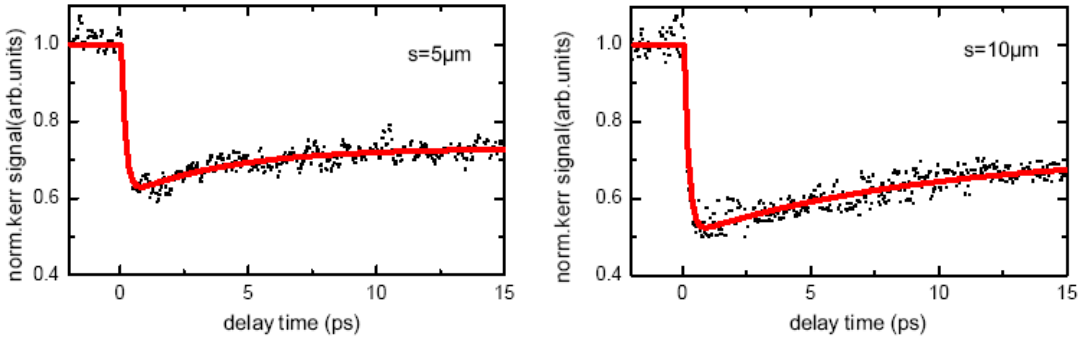

(a) (b)

Figure 4.18: Demagnetization curves of the patterned arrays with 5µm dot diameter and separations of (a) 5 µm and (b) 10 µm.

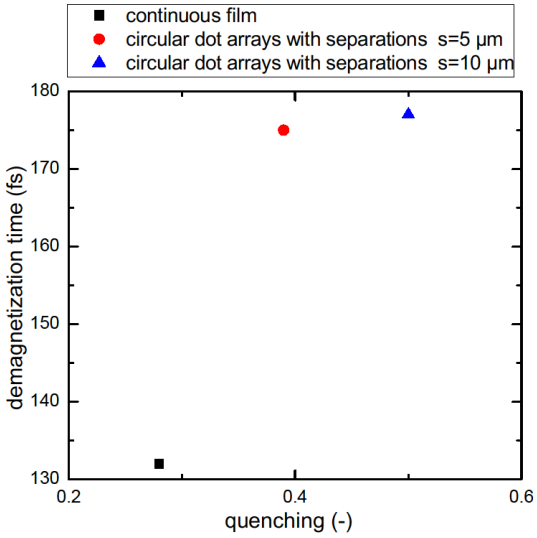

Figure 4.19: Demagnetization time reported for continues $Co_{65}Pd_{35}$ film (black square) compared to the demagnetization times of circular dot arrays with separations of 5µm (red circuit) and 10µm (blue triangle).

4.4 Ultrafast Demagnetization of Ni_xPd_{100-x} Films

The demagnetization curves for thin Ni_xPd_{100-x} samples ($35 \leq x \leq 65$) were measured at room temperature in the polar Kerr geometry, as shown in figure 4.20. The fluence of the pump-beam was approximately 6.50mJ/cm^2 for all samples.

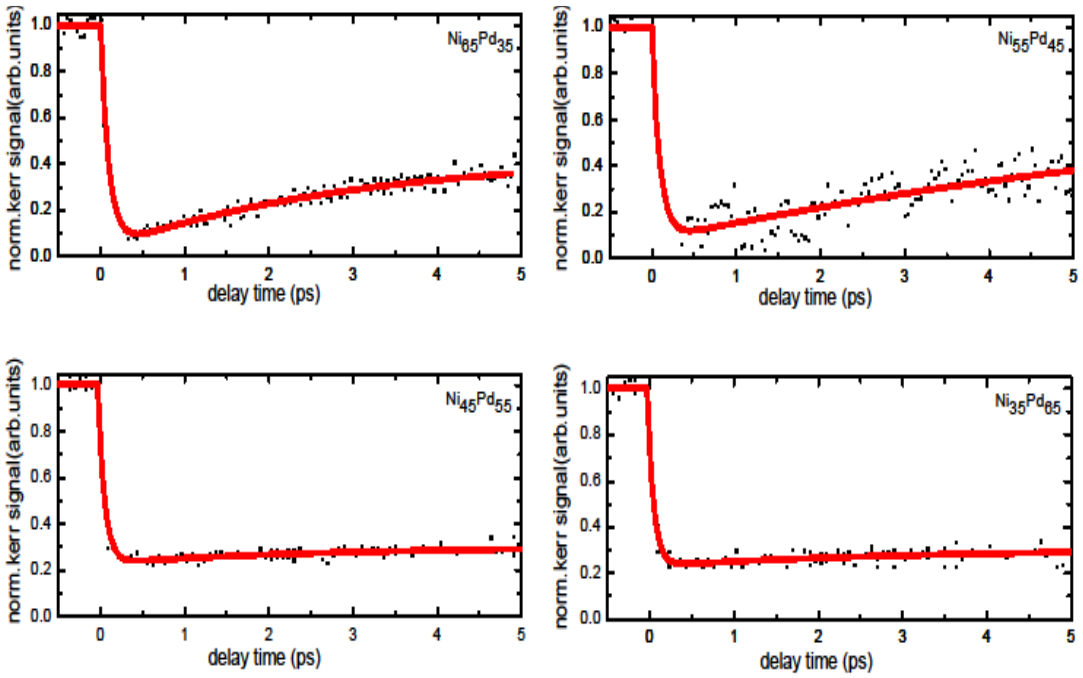

Figure 4.20: Demagnetization curves of different Ni_xPd_{100-x} samples ($35 \leq x \leq 65$). The measurements were carried out in polar Kerr geometry.

The quenching is significantly stronger $Ni_{65}Pd_{35}$ than $Co_{65}Pd_{35}$ at the same fluence. The samples $Ni_{45}Pd_{55}$ and $Ni_{35}Pd_{65}$ almost completely demagnetized after the excitation.

The demagnetization times extracted using the fitting function (4.1) are summarized in table (4.5) and also plotted in figure (4.21).

Sample	$Ni_{65}Pd_{35}$	$Ni_{55}Pd_{45}$	$Ni_{45}Pd_{55}$	$Ni_{35}Pd_{65}$
τ_M (fs)	94± 6	90± 12	83± 4	85± 15

Table 4.5: Demagnetization times of the Ni_xPd_{100-x} films of figure 4.20

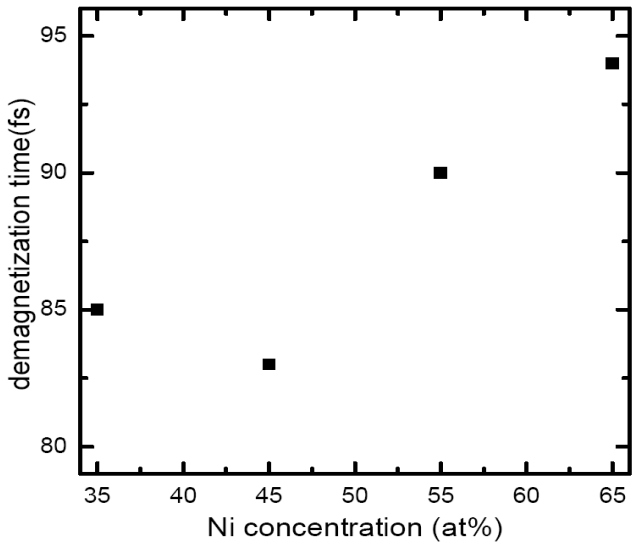

Figure 4.21: Measured demagnetization times for Ni_xPd_{100-x} films of table 4.3.

Chapter 5 Conclusions and Future Work

5.1 Summary of Conclusions

A. The Effect of Thickness, Size and ratio of Ni on the Magnetic Behavior of Ni films, Using L-MOKE Geometry.

1. The first series of the samples were Ni thin films on Si substrates. These were made with thickness in the range of 5-50 nm with and without capping layer (Al) of 5 nm. All samples in this series showed hysteresis loops with sharp transitions between the two saturation magnetizations, with transition tendency to become smoother with increasing the thickness. Both of these observations are attributed to the magneto-static energy. The coercivity also showed tendencies to increase with increasing thickness.
2. The second series consisted of Ni circular dots with diameters in the range 10-50μm. There is no significant influence of the diameter change on the Ni magnetic behavior.
3. The third series consisted of Ni_xPd_{100-x} with different Ni film ratio x ($35 \leq x \leq 65$). The coercivity magnetization increases as the sample Ni content increases.

B. Magnetic Properties of $Co_{65}Pd_{35}$ and Circular Dot Arrays

1. Using MFM, the magnetic domain of $Co_{65}Pd_{35}$ was found with an average domain size of 80 nm. From the domain configuration, the easy magnetization axis is out-of-plane rather than in-plane.
2. Using SQUID magnetometer, the hysteresis loop of $Co_{65}Pd_{35}$ was measured, and the magnetic moment at saturation is M_S = 495 emu/cc.
3. Using static MOKE in Polar geometry, the effect of interedot dipole coupling in $Co_{65}Pd_{36}$ dots arrays was studied. For the patterned arrays the coercivity Hc and saturation Hs were found to increase with increasing the inter element separation (s).

C. Demagnetization Dynamics of $Co_{65}Pd_{36}$ and Ni_xPd_{100-x} samples ($35 \leq x \leq 65$), Using Time-resolved MOKE in Polar Geometry.

1. Demagnetization processes were studied by recording the hysteresis loops of $Co_{65}Pd_{35}$ films at different times relative to the pump beam arrival. The magnetization strength showed a decrease within less than a picosecond after the pump beam arrival.

2. The double exponential function was used to estimate demagnetization time, recovery time, and quenching of the magnetization.
3. The effect of excitation fluences on demagnetization time of $Co_{65}Pd_{35}$ was studied by recording demagnetization curves at different pump-beam fluences. The demagnetization and recovery times become longer for increased pump fluences.
4. Ultrafast demagnetization of $Co_{65}Pd_{35}$ circular dots arrays was measured. Quenching increased with the separation increase from 5 to 10 μm.
5. Quenching was significantly stronger for $Ni_{65}Pd_{35}$ compared to $Co_{65}Pd_{35}$ under the same fluence.

5.2 Recommendations for Future Work

We recommend conducting the following tests and measurements as a follow-up to our work:

1. Study the effect of temperature on the magnetic behavior of Ni.
2. Study the effect of thickness, size and ratio of Ni on the Magnetic Behavior of Ni films, Using P-MOKE and V-MOKE geometry and compared with the measurements of L-MOKE geometry.
3. Study the effect of thickness, size and ratio of other samples, for example Co, Fe , CoPd , NiPd ….
4. Study the magnetic dynamic of $Co_{65}Pd_{35}$ ***square*** dots arrays, and compared with the measurements of $Co_{65}Pd_{35}$ ***circular*** dots arrays.
5. Study the effect of excitation fluences on demagnetization time of $Co_{65}Pd_{36}$ in L-MOKE geometry and compared with the measurements of P-MOKE geometry.

Bibliography

[Abelmann, 2005]. Leon Abelmann. *Principle of Magnetic Force Microscopy.* Netherlands: University of Twente ,(2005).

[Altissimoa, 2010]. Matteo Altissimoa. *E-beam lithography for micro-/nanofabrication.* American Institute of Physics, Biomicrofluidics 4, 026503, (2010).

[Armen, 2008]. G. Bradley Armen. *Phase sensitive detection: the lock-in*. Knoxville, Tennessee 37996-1200, (2008).

[Bader, 2006]. S. D. Bader. *Colloquium: Opportunities in nanomagnetism.* Rev. Mod. Phys. 78, 1, (2006).

[Beaurepaire et al, 1996]. E. Beaurepaire, J.C.Merle, A. Daunois, and J. Y. Bigot. *Ultrafast Spin Dynamics in Ferromagnetic Nickel.* The American Physical Society, Physical Review Letters 76:4250, (1996).

[Belov, 2004]. Miroslav Belov. *Spatiotemporal magnetization dynamics of patterned* $Ni_{80}Fe_{20}$, pp 11,12. Edmonton, Alberta: University of Alberta,(2004).

[Bitter, 1932]. Bitter, F. *Experiments on the nature of ferromagnetism*, Physical Review 41 (1932), pp 507-515, (1932).

[**Carpene et al, 2008]**. E. Carpene, E. Mancini, C. Dallera, M.Brenna, E.Puppin, and S.De Silvestri. *Dynamics of electron-magnon interaction and ultrafast demagne- tization in thin iron films*. Physical Review. B 78, 174422, (2008).

[Carva et al, 2011]. K. Carva, M. Battiato and P. M. Oppeneer. *Ab initio investigation of Elliott-Yafet electron-phonon mechanism.* Department of Physics and Astronomy,Uppsala, Sweden: Physical Review Letters, 107:207201, (2011).

[Chappert et al, 2007]. Claude Chappert, Albert Fert and Frédéric Nguyen Van Dau. The emergence of spin electronics in data storage. Nature materials, Vol 6, 813-823 (2007).

[ekspla,2011]. *Scanning Autocorrelator*. [Online; accessed 27-June-2014].
RUL: *http://www.ekspla.com/wp- content/uploads/2011/06/scanning_autocorrelator_AC.pdf*

[Fratta, 2012]. Giovanni Di Fratta. *On the nature of magnetization statesminimizing the micromagnetic free energy functional.* Università degli studi di Napoli "Parthenope, (2012).

[Gantz, Reinsel, 2012]. John Gantz , David Reinsel. *THE DIGITAL UNIVERSE IN 2020: Big Data, Bigger Digital Shadows, and Biggest Growth in the Far East* . I D C I V I E W (IDC 1414),(2012).

[Hendrych et al, 2007]. A.Hendrych, R.Kubínek and A.V. Zhukov. *The magnetic force microscopy and its capability for nanomagnetic nanomagnetic studies - The short compendium.* Modern

Research and Educational Topics in Microscopy. A. Méndez-Vilas and J. Díaz (Eds.) FORMATEX,(2007).

[Hubert, Schäfer,2000]. A.Hubert, R.Schäfer. *Magnetic Domains - The Analysis of Magnetic Microstructuers. In Magnetic Domains- The Analysis of Magnetic Microstructuers*, pp24,25. Erlangen, Dresden: Springer Verlag, (2000).

[Hujan, 2013]. Zulzawawi Bin Haji Hujan. *Magneto–Optical Kerr Effect Microscopy Investigation on Permalloy Nanostructures thesis*. University of York,Department of Physics, (2013).

[Kampen, 2003]. Maarten van Kampen. *Ultrafast spin dynamics in ferromagnetic metals*. Eindhoven: Technische Universiteit Eindhoven ,ISBN 90-386-1705-4 ,NUR 924,(2003)

[Kampfrath et al, 2002]. T. Kampfrath, R. G.Ulbrich,F. Leuenberger, M. Munzenberg, B. Sass, and W. Felsch. *Ultrafast magneto-optical response of iron thin films*. Göttingen, Germany, Physical Review B, Vol 65, 104429,(2002).

[Kimel et al, 2002] A.V. Kimel, R.V. Pisarev, J. Hohlfeld, and Th. Rasing. *Ultrafast Quenching of the Antiferromagnetic Order in $FeBO_3$: Direct Optical Probing of the Phonon-Magnon Coupling*. Physical Review letters, 89:287401, (2002).

[Kittel, 1949].Charles Kittel. *Physical Theory of Ferromagnetic Domains*.Review Modern. Physics. 21, 541, (1949).

[Koopmans, 2003]. Bert Koopmans. *Laser-Induced magnetization dynamic In;spin dynamics in confined magnetic structure* . Springer Berlin Heidelberg,Topics in Applied Physics,Volume 87, pp 256-323, Series ISSN 0303-4216, (2003).

[Koopmans et al, 2010]. B. Koopmans, G. Malinowski, F. Dalla Longa, D. Steiauf, M. Fähnle, T. Roth, M. Cinchett and M. Aeschlimann. *Explaining the paradoxical diversity of ultrafast laser-induced demagnetization*. , Nature Materials ,Vol 9,259-265,(2010).

[Landau and Lifshitz, 1935]. Landau, L.D, and Lifshitz, E. *On the theory of the dispersion of magnetic permeability in ferromagnetic bodies*, pp 153-169. Physikalische Zeitschrift der Sowjetunion 8, (1935).

[Longa, 2008]. Francesco Dalla Longa. *Laser-induced magnetization dynamics - an ultrafast journey among spins and light pulse*. Eindhoven: Technische Universiteit Eindhoven,ISBN 978-90-386-1279-9 NUR 926, (2008).

[Malaika,Nicola,2011]. Susan Malaika,Matthias Nicola. *Data normalization reconsid- ered, Part 1: The history ofbusiness records.An examination of record keeping in computer systems.* IBM Corporation, (2011).

[Masakatsu et al,2013]. H.Masakatsu, S. Hiroshi and S. Seiichi. *Trends in Technologies for HDDs, ODDs, and SSDs, and Toshiba's Approach*. TOSHIBA Storage Product for ICT Society, (2013).

[NDT, 2013]. *Graph of hysteresis loop*. [Online; accessed 30-June-2014]. NDT Resource Center. RUL: https://www.nde-ed.org/index_flash.htm

[Oppeneer, 2000]. P. M. Oppeneer. *Magneto-optical kerr spectra*. Institute of solid state and materials research, Germany 13:229–422,(2000).

[Paschotta,2008]. Rüdiger Paschotta. *Field Guide to Laser Pulse Generation*. Bellingham, Washington USA.SPIE: 9780819472489 Volume: FG14, (2008).

[Radu et al, 2009]. I. Radu, G. Woltersdorf, M. Kiessling, A. Melnikov,U. Bovensiepen, J.-U. Thiele, and C. H. Back. *Laser-Induced Magnetization Dynamics of Lanthanide-Doped Permalloy Thin Films*. Physical Review Letters 102 (11), 117201, (2009).

[Rullière,2005]. Claude Rullière. *Femtosecond Laser Pulses: Principles and Experim- ants*. 2nd Edition. Springer. SPIN 10925751, (2005).

[Shinjo,2009]. Teruya Shinjo. *Nanomagnetism and Spintronics*, First edition. The Boulevard, Langford Lane, Kidlington, Oxford, OX5 1GB, UK: Elsevier, ISBN: 978-0-444-53114-8, (2009).

[Sixtus and Tonks, 1931].K. J. Sixtus and L. Tonks. *Propagation of large Barkhausen discontinuities* ,Physical Review 37 (1931), pp 930-958. (1931).

[Spectra Physics, 2001]. *Millennia User's Manual*. Mountain view, CA, USA): Spectra Physics, The Solid-State Laser Company. Mountain View, CA 94043. Part Number 0000-245A, Rev. D, (2001).

[Spectra Physics 01, 2002]. *Tsunami User's Manual.* Mountain view, CA, USA): Spectra-Physics, The Solid-State Laser Company. Mountain View, CA 94043. Part Number 0000-232A, Rev. D, (2002).

[Spectra Physics02, 2002]. *Empower User's Manual*. Mountain view, CA, USA): Spectra-Physics, The Solid-State Laser Company, (2002).

[Spectra Physics.2005]. *Spitfire Pro User's Manual*. Mountain view, CA, USA): Spectra-Physics,The Solid-State Laser Company. Mountain View, (2005).

[Stöhr, Siegmann, 2006]. Joachim Stöhr, Hans Christoph Siegmann. *Magnetism: From Fundamentals to Nanoscale Dynamics,Volume 152 of Springer Series in Solid-State Sciences, ISSN 0171-1873*. Stanford, (2006).

[**Sun et al, 2011**]. Li Sun, Pingkwanj Wong, Wen Zhang, Xiao Zou, Linqiang Luo, Ya Zhai, Jing Wu, Yongbing Xu, and Hongru Zhai. *The effect of interelement dipole coupling in patterned ultrathin single crystal Fe square arrays*. American Institute Physics: Journal of Applied Physics 109, 033913,2011, (2011).

[Trudel et al, 2010].Trudel.S, Georg Wolf, Helmut Schultheiß, Jaroslav Hamrle,Burkard Hillebrands,Takahide Kubota, and Yasuo Ando. *Note: Probing quadratic magneto-optical Kerr effects with a dual-beam system.* Review of Scientific Instruments 81, 026105,(2010).

[Tseng et al, 2003]. Ampere A. Tseng, Kuan Chen, Chii D. Chen, and Kung J. Ma. *Electron beam lithography in nanoscale fabrication: recent development.* (Volume: 26), Tempe, AZ, USA: Electronics Packaging Manufacturing, IEEE Transactions on 2003.

[Tsymbal, 2014]. E.Y.Tsymbal, *Introduction to Solid State Physics lecture (section 16: Section 16: Magnetic properties of materials),* University of Nebraska–Lincoln, 2012.
RUL:
http://unlcms.unl.edu/cas/physics/tsymbal/teaching/SSP-927/Section%2016_Magnetic_Properties_2.pdf

[Vahaplar, 2011].Vahaplar. *Ultrafast Path for Magnetization Reversal in Ferrimagnetic GdFeCo Films*. Ipskamp, Enschede, The Netherlands.ISBN/EAN: 978-94-91211-78-2, (2011).

[Wang, 2008 et al]. J.Wang, L. Cywinski, C. Sun, J. Kono, H. Munekata, and L. J. Sham. *Femtosecond demagnetization and hot-hole relaxation in ferromagnetic $Ga1_{1-x}Mn_xAs$*.. Physic Review, 77:235308, (2008).

[Weinberger, 2008] P. Weinberger. *John Kerr and his effects found in 1877 and 1878*. Philosophical Magazine Letters, 88:12, 897-907, (2008).

[Weiss, 1906]. Weiss, P. *The hypothesis of the molecular field and the property of ferromagnetism.*, pp 661-690. (1906).

[Wikipedia, 2009] *Magnetic force microscopy (MFM).* [Online; accessed 11-June-2014].
RUL:http://en.wikipedia.org/wiki/Atomic_force_microscopy#mediaviewer/File:Atomic_force_microscope_block_diagram.svg

[Wikipedia,2013] *Wollaston prism*. [Online; accessed 29-June-2014].

RUL http://en.wikipedia.org/wiki/Wollaston_prism

[Xu et al, 2001] Y. B. Xu, A. Hirohata, S. M. Gardiner, M. Tselepi, J. Rothman, M. Kläui, L. Lopez- Diaz, J. A. C. Bland, Y. Chen,E. Cambril, and F. Rousseaux. *Effects of Interdot Dipole Coupling in Mesoscopic Epitaxial Fe(100) Dot Arrays*. IEEE, Transactions on Magnetics, Vol. 37,2055-2057 NO. 4, (2001).

[Yaminsky, Tishin, 1999] I.V.Yaminsky and A.M.Tishin. *Magnetic force microscopy*. Russia: Russian Academy of Sciences and Turpion Ltd. Russian Chemical Reviews 68 (3) 165 ± 170, (1999).

[Zhang et al, 2005] F. Zhang, C. Xu, P. M. Hui, and Y. Q. Ma. *Influence of dipolar interaction on small magnetic dot arrays*. Journal of Applied Physics 97, 103912; doi: 10.1063/1.1900930, Published by the AIP Publishing, (2005).

الملخص

بهاء الدين محمود أبو ريش

باشراف الدكتور سلمان محمد سلمان

وكلاوس شنايدر من مركز ابحاث يولش في المانيا

تم في هذا البحث دراسة موسعة للديناميكيات المغناطيسية لعدد من سطوح الرقائق باستخدام ظاهرة كير المغنيتو ضوئية (موك). وتم في البدء استخدام جهاز كير لدراسة تأثير سمك ومساحة الرقائق على السلوك المغناطيسي لمعدن النيكل.

ومن ثم تمت دراسة الديناميات المغناطيسية لرقائق من مركب $Co_{65}Pd_{36}$ باستخدام ميكروسكوب القوة المغناطيسية وجهاز التداخل الكمي فائق الإيصالية (سكويد) بالإضافة إلى جهاز ظاهرة كير المغنيتو ضوئية (موك).

وقد تم فحص رقائق من مصفوفات نقطية من مركب $Co_{65}Pd_{35}$ مثبتة على قواعد من السليكون لدراسة اعتمادية الإجبارية للمركب وتوزيعه على المسافة بين النقاط وأنصاف أقطارها. وقد تبين وجود الاعتمادية والتي نتجت عن تفاعلات بين المغانط ثنائية القطبية وارتباط ذلك بعملية فقدان المغنطة وعملية استرجاعها بعد فقدانها المؤقت بسبب نبضات الليزر.

وتم استخدام ظاهرة كير المغنيتو ضوئية فائقة التوقيت من خلال استخدام تقنية تفاعل موجتي المرجعية والفحص ضمن منظومة كير لدراسة ديناميات عملية فقدان المغنطة فائقة السرعة لمركبات Ni_xPd_{100-x} و $Co_{65}Pd_{35}$ وتبين وجود تأثير لتوزيع المنظومة الهندسي للمركب على هذه الديناميات بالإضافة إلى تأثيرات أخرى تتعلق بازدياد زمن فقدان المغنطة واسترجاعها مع تزايد قيمة الضخ الليزري. وقد تمت مقارنة المعطيات المقاسة مع نموذج *Koopmans et al* حيث تحقق انسجام في بعض القضايا واعتماد كبير لذلك على نسبة عنصر البوليديوم Pd ضمن العينات.

نوصي بدراسة نماذج أخرى شبيهة من خلال مشاركات بنفس المركز.